



HAL
open science

Size-independent strain gradient effective models based on homogenization methods: Applications to 3D composite materials, pantograph and thin walled lattices

Ahmed Lahbazi, Ibrahim Goda, Jean-François Ganghoffer

► To cite this version:

Ahmed Lahbazi, Ibrahim Goda, Jean-François Ganghoffer. Size-independent strain gradient effective models based on homogenization methods: Applications to 3D composite materials, pantograph and thin walled lattices. *Composite Structures*, 2022, 284, pp.115065. 10.1016/j.compstruct.2021.115065 . hal-04145521

HAL Id: hal-04145521

<https://hal.univ-lorraine.fr/hal-04145521>

Submitted on 22 Jul 2024

HAL is a multi-disciplinary open access archive for the deposit and dissemination of scientific research documents, whether they are published or not. The documents may come from teaching and research institutions in France or abroad, or from public or private research centers.

L'archive ouverte pluridisciplinaire **HAL**, est destinée au dépôt et à la diffusion de documents scientifiques de niveau recherche, publiés ou non, émanant des établissements d'enseignement et de recherche français ou étrangers, des laboratoires publics ou privés.



Distributed under a Creative Commons Attribution - NonCommercial 4.0 International License

Size-independent strain gradient effective models based on homogenization methods: Applications to 3D composite materials, pantograph and thin walled lattices

Ahmed Lahbazi¹, Ibrahim Goda², Jean-François Ganghoffer¹

¹LEM3 – Université de Lorraine – CNRS. 7, rue Félix Savart. 57073 Metz Cedex, France

²Université Bourgogne Franche-Comté, FEMTO-ST Institute, Département Mécanique Appliquée, 24 rue de l'Épitaphe, 25000 Besançon, France

E-mail addresses: ibrahim.goda02@gmail.com; Ibrahim.goda@femto-st.fr (I. Goda)
Ahmed.Lahbazi@univ-lorraine.fr (A.Lahbazi), jean-francois.ganghoffer@univ-lorraine.fr (J.-F. Ganghoffer)

ARTICLE

INFO

Keywords: Homogenization;
Strain gradient continua;
Variational principles;
Composite materials; Thin-walled lattice materials;
Effective moduli; Hill-Mandel macrohomogeneity condition.

ABSTRACT

The notion of strain gradients provides a reliable model for capturing size effects and localization phenomena. The difficulty in identifying corresponding constitutive parameters, on the other hand, restricts the practical applicability of such theory. In this work, we aim at developing homogenization based strain-gradient continuum models to compute the effective Cauchy and strain gradient moduli for a wide class of 3D architected materials and composites prone to strain gradient effects. The present homogenization method is based on a variational principle in linear elasticity articulated with Hill's lemma, which is extended by considering the generalized kinematics within the framework of periodic homogenization. The microscopic displacement field is decomposed into a polynomial function of the introduced macroscopic kinematic variables and the other is periodic fluctuation. The fluctuating displacement is expressed versus the macroscopic kinematic variables solving sequential classical and higher order unit cell boundary value problems. The computed effective elastic moduli in the current computing framework do not depend on the unit cell size, and are therefore intrinsic to the microstructure within the structure. 3D applications for inclusion based composites, pantographic lattices and thin-walled lattice structures are carried out in order to exemplify the proposed homogenization strategy, showing pronounced strain gradient

1. Introduction

The modeling of materials with a heterogeneous microstructure sometimes requires richer and more efficient models than the classical first order formulation to describe and predict the effective homogeneous behavior at the macroscopic scale [1]. Higher order formulations are needed to better describe the macroscopic behavior law, these last ones consider not only the local deformation but also the variation of the deformation field, this allows us to have non-local information [2-4]. Higher gradient formulations are also able to assess the impact of the

geometry and properties of each component of the microstructure on the macroscopic scale response for a homogeneous substitution continuum. Since experimental determination of the effective properties of heterogeneous microstructure materials is delicate, predictive micromechanical models could be employed to determine the macroscopic behavior of the heterogeneous structures at a given loading mode. Likewise, optimizing the design of such materials necessitates a grasp of the relationship between internal architecture and physical characteristics, along with adequate methods for evaluating these properties.

The extension of the classical theory of linear elasticity based on Cauchy, gives formulations of higher order and higher gradient continua. This extension implies respectively additional degrees of freedom like the Cosserat medium proposed by the Cosserat brothers [5], or the advanced micromorphic medium [6-8], and higher gradients of the selected primary variables, a kind of weak non-locality. Indeed, additional constitutive tensors and parameters are required for generalized continuum mechanical theories, which are generally non-intuitive and difficult to acquire experimentally. As a result, homogenization methodologies have been developed to quantitatively calculate the relevant parameters for a particular microstructure [9-12], because of the growing interest in metamaterials, numerous recent researches have tackled homogenization methods for periodic microstructures. It is critical to have an accurate and efficient prediction of mechanical properties when designing and fabricating metamaterials for engineering applications [13,14]. Finite element methods may be used to model a structure down to the smallest detail of its components. However, this necessitates a mesh size at least one order lower than the geometric size of the substructure, resulting in extremely high computational costs. Therefore, homogenization approaches are being developed in order to upscale the mechanical response at the microscale to the macroscale by establishing an appropriate constitutive equation at a tractable numerical cost. Using additive manufacturing technology, a structure at the macroscale with a lattice substructure of micrometer dimensions can be created. At the macroscale, such a system is referred to as a metamaterial since its mechanical properties differ from those at the microscale. As a result, the metamaterial is modeled using supplementary parameters, whereby the micro to macroscale constitutive relations can be established using a homogenization strategy. A classical homogenization with the same-grade theory at both scales fails to capture size effects. A viable strategy is therefore important to use a higher gradient theory to describe the size effects in materials due to the inherent microstructure, and to determine additional macroscale parameters. The higher-grade theories and homogenization within that framework

are a challenging endeavor undertaken by several scientists, including [15-19]. In most scenarios, it is acknowledged that homogenization of Unit Cell (UC) by including the so-called higher gradient terms of the macroscopic field is a natural scheme to incorporate the size effect [20,21]. A fascinating class of structures that may be characterized at the macroscale using a second gradient theory are pantographic structures. They have received great attention in the literature[22-25] especially from a rigorous mathematical point of view. One of our main concerns in this contribution is to describe the pantograph structures based on second gradient formulations.

Nowadays composite materials are very useful in aeronautical, automotive, and other applications, due to their numerous advantages, including high mechanical properties and strength, energy absorption capabilities, thermal and acoustic insulation. Hence, predictive approaches for these materials are needed in order to bridge the scales and to provide a constitutive law at a continuum scale, whereby the equivalent continuum properties can be related to both the geometrical and mechanical microstructural parameters of the structure. Furthermore, designing such kind of materials in an optimal way requires understanding at the same time the relation between the internal architecture and physical properties. On the other hand, the effective micromechanical modelling seems to be efficient and very useful in the last decades. The homogenization of these heterogeneous materials is based on the calculation of the volume average on a repetitive or periodic unit cell. The effective properties calculated from appropriate homogenization schemes show the influence of the geometrical and mechanical microstructural parameters of the composite constituents. The classical homogenization is based on a scale separation assumption, known as the Hill-Mandel macrohomogeneity condition[26, 27]. Nonlocal theories have been proposed to address this issue. The widespread adoption of these approaches can be attributed to the ability to overcome the limitations of structural theories based on classical elasticity.

Higher gradient formulations are necessary, which accounts for not only the local strain of the material, but also the variation of the strain field, and therefore nonlocal information [2] (Lim, Zhang & Reddy, 2015). There is a large body of works in the literature dealing with strain gradient models, starting more than two decades ago [28-35], for the composite with periodic or random microstructures we find the work of [36], auxetic architected materials [37] or random fibrous media [38]. To the best of our knowledge, no previous work has looked at the modeling of lattice structures and metamaterials in a 3D perspective using strain gradient continua and explored the dependence of the homogenized constitutive models on the

microstructural parameters. The modeling of second gradient medium in a 3D context will be an advantage for geometries that are not feasible and not projectable in 2D, like for thin-walled lattice structures. The development of the theory of strain gradient in 3D allows us to have very rich models. These models then make it possible to test even complex geometries in various loading modes.

Few works in the literature deal with 3D analyses of the higher-grade behavior of composites or architected materials, and most of the proposed works are set for 2D geometries, mostly due to the inherent complexity of meshing such geometries and computing the entire set of higher gradient moduli. Moreover, while higher gradient effects are due to the strong contrast of mechanical properties of the constituents within the unit cell, interactions between neighboring unit cells are in fact not taken into account in most of the existing models of the literature (leading to a macroscopic distortion of the microstructure), despite this effect being the expected manifestation of higher gradient mechanics. Composites show strain gradient effects that are most of the time not very significant, as the typical boundary layer zone has a size (quantified by the internal lengths of the strain gradient constitutive model) that is much lower compared to the unit cell size. The present work exhibits the following novel aspects:

- A sound strain gradient mechanics homogenization framework is proposed for 3D periodic structures, including composites and thin-walled lattice structures;
- The size-independency of the higher gradient properties is fulfilled by the proposed method after proper normalization of higher gradient moduli;
- We design pantograph-type microstructures prone to significant strain gradient effects;
- True strain gradient effects are triggered thanks to the application of double forces; this feature being exemplified for the pantograph structure;
- The accuracy of the strain gradient substitution continuum is assessed by an energetic analysis, considering especially the relative importance of the energy of the fluctuation quantifying the discrepancy between the postulated effective strain gradient medium and the initially heterogeneous microstructure.

The remainder of this contribution is organized as follows. Section 2 provides the general methodology for the determination of the effective strain gradient properties of heterogeneous materials on the basis of homogenization methods and presents the theoretical formulation of this proposed method which aims to identify the effective strain gradient continuous behavior.

A pantographic structure is used to analyze and validate the strain gradient model in section 3. Numerical 3D examples are selected in the second part of the paper, considering pantographic structures (section 3), inclusion-based functionally graded composites (section 4) and thin-walled materials (section 5) to illustrate the proposed homogenization methodology and to perform a sensitivity analysis of the effective moduli to the geometrical and mechanical microstructural parameters. A summary of the main results and perspectives for future work concludes the paper in section 6.

A few words regarding the employed notations are in order. The physical space is embedded within the Euclidean space and vectors and higher order tensors are implicitly decomposed into an orthonormal basis of the underlying vector space. Vectors and tensors are denoted by boldface symbols. We denote the microscopic quantities with lower case letters, like \mathbf{u} , the micro-displacement, and with upper case letters the corresponding macroscopic quantities like \mathbf{U} , the macro displacement. The gradient of a scalar or tensor field with respect to the position is denoted with the nabla operator and the position as a subscript, viz.. $\nabla_{\mathbf{x}}\mathbf{E}(\mathbf{x})$, represents the gradient of the tensor field $\mathbf{E}(\mathbf{x})$ w.r.to the macroscopic position, vector \mathbf{x} . The transpose of a tensor is written with a superscript notation, for instance \mathbf{B}^T ; the transpose of a third order tensor applies to its two last indices. The gradient of a tensor field $\mathbf{A}(\mathbf{y})$ is denoted $\mathbf{A}(\mathbf{y}) \otimes \nabla_{\mathbf{y}}$ (with \otimes the tensor product) and its divergence is obtained as the trace of the gradient, denoted $\mathbf{A}(\mathbf{y}) \cdot \nabla_{\mathbf{y}}$. The vector product of two vectors or tensors \mathbf{U} , \mathbf{V} is denoted $\mathbf{U} \times \mathbf{V}$. The transpose of any third order tensor \mathbf{D} with components D_{ijk} in a Cartesian basis is the tensor D^T with components D_{ikj} in the same basis. The symmetrized dyadic product is denoted \otimes^s . The dot product therein represents the internal product in the space of Cartesian tensors. The simple, double and triple contractions of tensors are written ‘.’, ‘..’ respectively. The vector product of two vectors or tensors \mathbf{U} , \mathbf{V} is denoted $\mathbf{U} \times \mathbf{V}$. The transpose of any third order tensor \mathbf{G} with components G_{ijk} in a Cartesian basis is the tensor \mathbf{G}^T with components G_{ikj} in the same basis. The strain field is defined as the symmetrical part of the displacement gradient, $\varepsilon_{\mathbf{x}}(\mathbf{u}) = \frac{1}{2} (\nabla_{\mathbf{x}}\mathbf{u} + \nabla_{\mathbf{x}}^T\mathbf{u})$. The averaging of a microscopic quantity over a spatial domain V is denoted by $\langle \sigma \rangle = \frac{1}{|V|} \int_V \sigma \, dV$.

We use in this paper a few abbreviations of the technical terms, which are standard in homogenization methods:

UC: Unit Cell

PBC: Periodic Boundary Conditions.

RVE: Representative Volume Element.

BVP: Boundary Value Problem

SG: Strain Gradient

HSP: Homogenization of Periodic Structures

SM: Statistical Modeling

HD: Homogeneous Displacement

FD: Fluctuation Displacement

2. Theoretical formulation of strain-gradient homogenization

In the case of periodic composite materials, the homogenization methods are based on two distinct scales: the scale of the microstructure for which the microscopic position is denoted y , and the macroscopic scale with the spatial position x . An implicit dependence on the macroscopic position is valid for the macroscopic deformation and its gradient, successively $E = E(x)$, $K = K(x)$. Here and in the following, the vectors y and x respectively denote the microscopic and macroscopic spatial positions of the material points; all positions are defined with respect to a fixed Cartesian basis; $Y(y)$ and $V(X)$ are respectively the volumes of the microscopic unit cell and of the macroscopic homogeneous medium, both shown in Fig. 1.

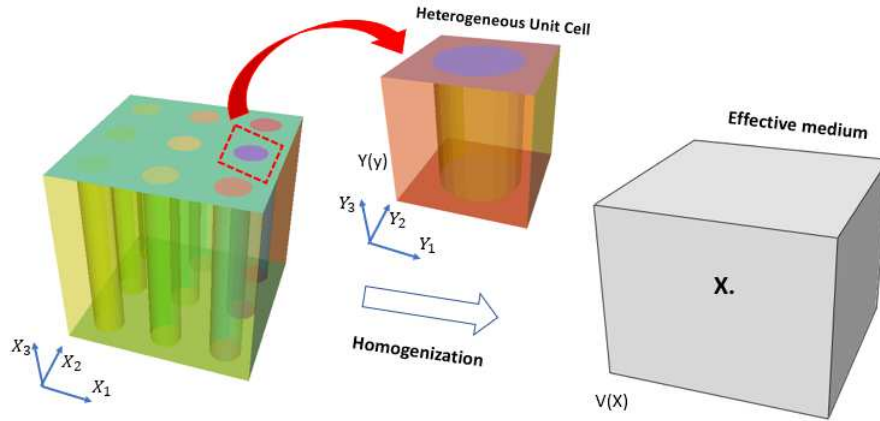


Figure 1: Unit cell of heterogeneous materials and its effective medium.

Homogenization methods are very efficient to predict and approximate the effective behavior of heterogeneous materials. These materials present heterogeneities in different areas in the structure to be studied; theoretically, it is not possible to consider the heterogeneities one by one. The problem turns out to be difficult to solve, because the description of these materials is only possible "on average": the ideal is to replace them by a macroscopically equivalent continuous medium, these materials being described by a continuous homogenized (also called equivalent or effective medium). In the following, the microscopic or local scale is the scale of heterogeneities and the macroscopic scale is the scale of the homogenized microstructure. The description of the macroscopic behavior can be obtained either by a phenomenological or experimental study, directly at the macroscopic scale, or by a homogenization technical, that is to say by passing from the microscopic description to the macroscopic description (scale transition). Among the types of homogenization, we find the homogenization of periodic structures (HSP) [39,40], and statistical modeling (MS) developed by Kroner [41] for materials random structures. The calculation of the effective properties by the methods of homogenization of heterogeneous materials is done over a periodic unit cell (UC), this UC represents the heterogeneity of the initial microstructure which is periodic in a regular way in all directions.

First order Cauchy based theories are valid under a strict condition of scale separation, but they fail in situations for which the wavelength of the loading becomes comparable to the size of the underlying microstructure. Despite its wide use, classical Cauchy theory proves unable to predict the overall behavior of the microstructure where the strict scale separation

hypothesis fails. The absence of a material length scale parameter in the classical theory of continuous elasticity, however, leads to an inaccurate description of macroscopic structural behaviors [11]. The objective of homogenization methods towards generalized continua is to remedy the limitations of classical homogenization techniques and to extend the field of validity of the continuum approach beyond the strict assumption of scale separation [6,7].

At the microscopic scale of the unit cell (UC) of the heterogeneous composite, a first gradient isotropic linear elasticity constitutive law is adopted, which together with the other field equations write:

$$\boldsymbol{\sigma} \cdot \nabla_y + \mathbf{b} = 0 \quad \text{in } Y \quad (1)$$

$$\boldsymbol{\sigma} \cdot \mathbf{n} = \mathbf{t} \quad \text{on } \partial Y \quad (2)$$

$$\boldsymbol{\sigma} = \mathbf{C} : \boldsymbol{\varepsilon} \quad (3)$$

The linearized strain tensor is the symmetrical part of the displacement gradient, this tensor is obtained by deriving the microscopic displacement with the respect to the micro-position y , the linearized strain tensor being the symmetrical part of the displacement gradient.

$$\boldsymbol{\varepsilon} := \mathbf{u} \otimes^S \nabla_y \quad (4)$$

From the isotropy property, the three-dimensional constitutive relation (Eq. 3) is given explicitly as follows:

$$\begin{bmatrix} \sigma_{11} \\ \sigma_{22} \\ \sigma_{33} \\ \sqrt{2}\sigma_{23} \\ \sqrt{2}\sigma_{13} \\ \sqrt{2}\sigma_{12} \end{bmatrix} = \begin{bmatrix} 2\mu + \lambda & \lambda & \lambda & 0 & 0 & 0 \\ \lambda & 2\mu + \lambda & \lambda & 0 & 0 & 0 \\ \lambda & \lambda & 2\mu + \lambda & 0 & 0 & 0 \\ 0 & 0 & 0 & 2\mu & 0 & 0 \\ 0 & 0 & 0 & 0 & 2\mu & 0 \\ 0 & 0 & 0 & 0 & 0 & 2\mu \end{bmatrix} \begin{bmatrix} \varepsilon_{11} \\ \varepsilon_{22} \\ \varepsilon_{33} \\ \sqrt{2}\varepsilon_{23} \\ \sqrt{2}\varepsilon_{13} \\ \sqrt{2}\varepsilon_{12} \end{bmatrix} \quad (5)$$

The Cauchy stress presents a material symmetry $\boldsymbol{\sigma} = \boldsymbol{\sigma}^T$ (this symmetry being a consequence of the angular momentum equilibrium), \mathbf{b} (Eq. 3) is the body force vector, \mathbf{n} the external normal vector of unit length, the tension vector and the microscopic stiffness tensor of the fourth order. The symmetry of Cauchy stress tensor results from the equilibrium of the angular momentum at the microlevel. The determination of the effective behavior of periodic composite materials is done by averaging the microscopic quantity over the unit cell, each describing the heterogeneities of the initial microstructure. This procedure leads to an

effective continuous medium at the macroscopic scale based on the evaluation of the mechanical response of a unit cell.

The center of area of the unit cell (UC in short), point \mathbf{x} defined with respect to the adopted Cartesian basis, is defined by the following integral relation.

$$\frac{1}{|Y|} \int_Y (\mathbf{y} - \mathbf{x}) dV_y = \mathbf{0} \quad (6)$$

wherein $|Y|$ denotes the unit cell area in a 2D context and its volume in 3D. The integration is done on all the microscopic points with the position vector within the UC, the meaning of relation (8) is that the relative position $\xi := (\mathbf{y} - \mathbf{x})$ of the microscopic points is of zero average over the unit cell.

2.1. Derivation of the effective Cauchy and strain gradient moduli

Periodic boundary conditions are considered, whereby a macroscopic strain $E(\mathbf{x})$ and a strain gradient $K(\mathbf{x})=E(\mathbf{x}) \otimes \nabla_{\mathbf{x}}$ are imposed as controlled kinematic variables over the UC boundary (Fig 1). In order to link the micro and macroscales, the microscopic displacement is decomposed into a quadratic form of the macroscopic kinematic variables representing the so-called homogeneous part u_i^{hom} , and it is corrected by a fluctuation displacement $\tilde{u}_i(\mathbf{y})$, nil on the UC boundaries:

$$u_i = u_i^{hom} + \tilde{u}_i = E_{ij} \cdot y_j + \frac{1}{2} K_{ijk} : (y_j \otimes y_k) + \tilde{u}_i(\mathbf{y}) \quad (7)$$

The macroscopic strain and the introduced macroscopic kinematic variables are linked by localization functions $H_{ijk}^E(\mathbf{y})$, $H_{ijkl}^K(\mathbf{y})$, such that it holds

$$\tilde{u}_i(\mathbf{y}) = H_{ijk}^E(\mathbf{y}) : E_{jk} + H_{ijkl}^K(\mathbf{y}) : K_{jkl} \quad (8)$$

The microscopic strain field expresses as:

$$\varepsilon_{ij} = \frac{1}{2} (u_{i,j} + u_{j,i}); \quad (9)$$

Eq.(7) entails the following decomposition of the microstrain tensor into a homogeneous and fluctuating contributions:

$$\varepsilon_{ij} = E_{ij} + \frac{1}{2}K_{ijk}y_k + \tilde{\varepsilon}_{ij}(y); \quad K_{ijk} = \varepsilon_{ij,k} = \frac{1}{2}(u_{i,jk} + u_{j,ik})$$

(10)

wherein $\tilde{\varepsilon}_{ij}(y) = \frac{1}{2}(\tilde{u}_{i,j} + \tilde{u}_{j,i})(y)$ is the strain fluctuation.

We observe that the strain field exhibits a total symmetry of the indices, in the 6 components, as indicated in its vector representation; similarly, the symmetry in the last two indices of the strain gradient tensor allows to represent it in vector format, as subsequently explained:

$$\varepsilon_{ij} = \varepsilon_{ji}; \quad K_{ijk} = K_{ikj}.$$

In the strain gradient continuum theories, the strain energy is written as a bilinear form of the kinematic variables, subsequently adopting a small strains formulation (the energies can therefore be expressed as quadratic functions of their kinematic arguments):

$$W_M(E, K) = \langle W_\mu(\varepsilon) \rangle = \langle \frac{1}{2} \varepsilon_{ij}(y) : c_{ijkl}(y) : \varepsilon_{kl}(y) \rangle = \frac{1}{2} E_{ij} : C_{ijkl}^{hom} : E_{kl} + \frac{1}{2} K_{ijk} : A_{ijklmn}^{hom} : K_{lmn} + E_{ij} (B_{ijklm}^{hom} + B_{ijklm}^{hom,T}) : K_{klm}$$

(11)

wherein c_{ijkl} and C_{ijkl}^{hom} , are respectively the tensors of microscopic and macroscopic first gradient elastic moduli, A_{ijklmn}^{hom} the components of the sixth order tensor of strain gradient moduli, and B_{ijklm}^{hom} the fifth order tensor of coupling moduli between first and second gradient behaviors. Relation (11) is the extended Hill macrohomogeneity condition, stating the identity of the average of the microscopic energy to the macroscopic energy density of the strain gradient effective continuum.

The evaluation of the homogenized macroscopic stress tensors for the strain gradient medium is done by deriving the strain energy with respect to the macro strain tensor $E(X)$ and the strain gradient tensor $K(X)$ respectively, leading to the following homogenized constitutive law:

$$\Sigma_{ij} = C_{ijkl}^{hom} : E_{kl} + B_{ijklm}^{hom} : K_{klm}$$

(12)

$$S_{ijk} = B_{ijklm}^{hom} : E_{lm} + A_{ijklmn}^{hom} : K_{lmn}$$

The matrix coefficients effective elastic Cauchy and strain gradient moduli, C_{ijkl}^{hom} , A_{ijklmn}^{hom} , and of the coupling matrix with components B_{ijklm}^{hom} , enjoy the following index permutation symmetry properties:

$$C_{ijkl}^{hom} = C_{jikl}^{hom} = C_{klij}^{hom}; \quad B_{ijklm}^{hom} = B_{jiklm}^{hom} = B_{ijlkm}^{hom}; \quad A_{ijklmn}^{hom} = A_{jiklmn}^{hom} = A_{lmnijk}^{hom}$$

In the case where the microstructure of the material presents a central symmetry, the fifth-order coupling elastic stiffness tensor B_{ijklm}^{hom} vanishes, so that the previous constitutive law becomes uncoupled in the form:

$$\Sigma_{ij} = C_{ijkl}^{hom} : E_{kl}$$

$$S_{ijk} = A_{ijklmn}^{hom} : K_{lmn}$$

(13)

Using the homogenized effective elastic moduli, we write the constitutive law for Cauchy and second gradient behaviors in a 2D context, relating the stresses and hyperstress to the strain and strain gradient tensors respectively, considering their index symmetries and in vector format. This leads to three independent components for the Cauchy medium and six independent components for the second gradient medium, adopting Bechterew basis [8] as follows:

$$E = [E_{11}, E_{22}, \sqrt{2}E_{12} = \sqrt{2}E_{21}]^T, \quad \Sigma = [\Sigma_{11}, \Sigma_{22}, \sqrt{2}\Sigma_{12} = \sqrt{2}\Sigma_{21}]^T \quad (14)$$

$$K = (K_{111}, K_{221}, \sqrt{2}K_{122}, K_{222}, K_{112}, \sqrt{2}K_{121})^T, \quad S = (S_{111}, S_{221}, \sqrt{2}S_{122}, S_{222}, S_{112}, \sqrt{2}S_{121})^T$$

(15)

The macroscopic stress and strain tensors are related by the homogenized constitutive law using notations from [18] as

$$\begin{pmatrix} \Sigma_{11} \\ \Sigma_{22} \\ \sqrt{2}\Sigma_{12} \end{pmatrix} = \begin{pmatrix} C_{1111}^{hom} & C_{1122}^{hom} & \sqrt{2}C_{1112}^{hom} \\ C_{2211}^{hom} & C_{2222}^{hom} & \sqrt{2}C_{2212}^{hom} \\ \sqrt{2}C_{1211}^{hom} & \sqrt{2}C_{1222}^{hom} & 2C_{1212}^{hom} \end{pmatrix} \begin{pmatrix} E_{11} \\ E_{22} \\ \sqrt{2}E_{12} \end{pmatrix}$$

(16)

$$(17) \quad \begin{pmatrix} S_{111} \\ S_{221} \\ \sqrt{2}S_{122} \\ S_{222} \\ S_{112} \\ \sqrt{2}S_{121} \end{pmatrix} = \begin{pmatrix} A_{111111}^{hom} & A_{111221}^{hom} & \sqrt{2}A_{111122}^{hom} & A_{111222}^{hom} & A_{111112}^{hom} & \sqrt{2}A_{111121}^{hom} \\ A_{221111}^{hom} & A_{221221}^{hom} & \sqrt{2}A_{221122}^{hom} & A_{221222}^{hom} & A_{221112}^{hom} & \sqrt{2}A_{221121}^{hom} \\ \sqrt{2}A_{122111}^{hom} & \sqrt{2}A_{122221}^{hom} & 2A_{122122}^{hom} & \sqrt{2}A_{122222}^{hom} & \sqrt{2}A_{122112}^{hom} & 2A_{122121}^{hom} \\ A_{222111}^{hom} & A_{222221}^{hom} & \sqrt{2}A_{222122}^{hom} & A_{222222}^{hom} & A_{222112}^{hom} & \sqrt{2}A_{222121}^{hom} \\ A_{112111}^{hom} & A_{112221}^{hom} & \sqrt{2}A_{112122}^{hom} & A_{112122}^{hom} & A_{112112}^{hom} & \sqrt{2}A_{112121}^{hom} \\ \sqrt{2}A_{121111}^{hom} & \sqrt{2}A_{121221}^{hom} & 2A_{121112}^{hom} & \sqrt{2}A_{121122}^{hom} & \sqrt{2}A_{121112}^{hom} & 2A_{121121}^{hom} \end{pmatrix} \begin{pmatrix} K_{111} \\ K_{221} \\ \sqrt{2}K_{122} \\ K_{222} \\ K_{112} \\ \sqrt{2}K_{121} \end{pmatrix}$$

The constitutive law writes in 3D space for the Cauchy effective medium considering the tensor index symmetries as shown below:

$$(18) \quad \begin{aligned} E &= [E_{11}, E_{22}, E_{33}, E_{12} = E_{21}, E_{23} = E_{32}, E_{13} = E_{31}]^T, \\ \Sigma &= [\Sigma_{11}, \Sigma_{22}, \Sigma_{33}, \Sigma_{12} = \Sigma_{21}, \Sigma_{23} = \Sigma_{32}, \Sigma_{13} = \Sigma_{31}]^T \end{aligned}$$

In the classical Cauchy formulation, there are 6 strain components E_{ij} and 6 Cauchy stress components Σ_{ij} , defined using the modified Voigt notation, i.e. by rewriting the 6 respective components of the tensors Σ and E as 2 column vectors, inducing the form of the 4th order tensor of elastic moduli simplified by material symmetry, as the following 6x6 matrix:

$$(19) \quad \begin{pmatrix} \Sigma_{11} \\ \Sigma_{22} \\ \Sigma_{33} \\ \Sigma_{12} \\ \Sigma_{23} \\ \Sigma_{13} \end{pmatrix} = \begin{pmatrix} C_{11}^{hom} & C_{12}^{hom} & C_{13}^{hom} & 0 & 0 & 0 \\ C_{21}^{hom} & C_{22}^{hom} & C_{23}^{hom} & 0 & 0 & 0 \\ C_{31}^{hom} & C_{32}^{hom} & C_{33}^{hom} & 0 & 0 & 0 \\ 0 & 0 & 0 & C_{44}^{hom} & 0 & 0 \\ 0 & 0 & 0 & 0 & C_{55}^{hom} & 0 \\ 0 & 0 & 0 & 0 & 0 & C_{66}^{hom} \end{pmatrix} \begin{pmatrix} E_{11} \\ E_{22} \\ E_{33} \\ E_{12} \\ E_{23} \\ E_{13} \end{pmatrix}$$

The 3D theory of strain gradient elasticity provides a vector of gradient of strain K_{ijk} which includes 18 components, conjugated in the sense of energy to the 18 components of the second gradient hyperstress tensor S_{ijk} . The constitutive relation between these two tensors delivers a matrix of homogenized strain gradient elastic moduli A_{ijklmn}^{hom} of size 18x18 (Fig. 2):

$$(20) \quad \begin{aligned} K_{ijk} &= [K_{111}, K_{221}, K_{122}, K_{331}, K_{133}, K_{222}, K_{112}, K_{121}, K_{332}, K_{233}, K_{333}, K_{113}, K_{131}, K_{223}, K_{232}, K_{231}, K_{132}, K_{123}]^T \\ S_{ijk} &= [S_{111}, S_{221}, S_{122}, S_{331}, S_{133}, S_{222}, S_{112}, S_{121}, S_{332}, S_{233}, S_{333}, S_{113}, S_{131}, S_{223}, S_{232}, S_{231}, S_{132}, S_{123}]^T \end{aligned}$$

The constitutive law of the second gradient in 3D is written in the following form:

The effective elastic moduli are formally expressed in terms of the first and second gradient strain localizers $A^E(y)$, $A^K(y)$, respectively the fourth and fifth order tensors defined versus the displacement localizers introduced in Eq. (8):

$$\begin{aligned} A^E(y) &:= I_4 + H^E(y) \otimes \nabla_y, \quad A^K(y) := (I_4 \otimes y + H^K(y) \otimes \nabla_y) \therefore T \rightarrow \tilde{\varepsilon}(y) = \\ A^E(y) &: E(x) + A^K(y) \therefore K(x) \end{aligned} \quad (22)$$

$$C^{hom} = \int_y A^E : C(y) : A^E dV_y$$

$$B^{hom} = \int_y (A^E(y))^T : C(y) \therefore A^K(y) dV_y \quad (23)$$

$$A^{hom} = \int_y (A^K(y))^T \therefore C(y) \therefore A^K(y) dV_y$$

In order to quantify the importance of second gradient effects, we compute the internal lengths, defined as the ratio of the constitutive homogenized second gradient parameters to those of the Cauchy first gradient constitutive model. We use the internal length definition as a second order tensor from [36], adopting the Voigt notation therein as follows:

$$le_{ij} = \sqrt{\frac{\sum_{r=1}^{r=2} A_{trjr}^{hom}}{C_{ij}^{hom}}} \quad (24)$$

2.2. Determination of the microscopic displacement and strain fields

The homogeneous part of the microscopic displacement which to be the exact solution for a heterogeneous body obeying the homogenized continuum of the postulated strain gradient is determined. Using Hill's lemma again, and based on the development of Eq.(7) and Eq. (10), we obtain the components of the vectors of microscopic displacement and strain field, for more details we refer to [4].

In a three-dimensional situation, the displacement and strain vectors write as follows:

$$u = [u_1, u_2, u_3]^T \quad (25)$$

$$\varepsilon = [\varepsilon_{11}, \varepsilon_{22}, \varepsilon_{33}, \varepsilon_{12} = \varepsilon_{21}, \varepsilon_{23} = \varepsilon_{32}, \varepsilon_{13} = \varepsilon_{31}]^T \quad (26)$$

$$u_1 = E_{11}x + E_{12}y + E_{13}z + \frac{x^2}{2} K_{111} + \frac{y^2}{2} K_{122} + \frac{z^2}{2} K_{133} + \frac{xy}{2} K_{112} + \frac{xz}{2} K_{113} + \frac{yz}{2} K_{123} + \tilde{u}_1$$

$$u_2 = E_{22}y + E_{21}x + E_{23}z + \frac{y^2}{2} K_{222} + \frac{x^2}{2} K_{211} + \frac{z^2}{2} K_{233} + \frac{xy}{2} K_{212} + \frac{xz}{2} K_{213} + \frac{yz}{2} K_{223} + \tilde{u}_2 \quad (27)$$

$$u_3 = E_{33}z + E_{31}x + E_{32}y + \frac{z^2}{2} K_{333} + \frac{x^2}{2} K_{311} + \frac{y^2}{2} K_{322} + \frac{xy}{2} K_{312} + \frac{xz}{2} K_{313} + \frac{yz}{2} K_{323} + \tilde{u}_3$$

$$\varepsilon_{11} = E_{11} + K_{111}x + \frac{y}{2} K_{112} + \frac{z}{2} K_{113} + \frac{\partial \tilde{u}_1}{\partial x}$$

$$\varepsilon_{22} = E_{22} + K_{222}y + \frac{x}{2} K_{212} + \frac{z}{2} K_{223} + \frac{\partial \tilde{u}_2}{\partial y}$$

$$\varepsilon_{33} = E_{33} + K_{333}z + \frac{x}{2} K_{313} + \frac{y}{2} K_{323} + \frac{\partial \tilde{u}_3}{\partial z}$$

$$\varepsilon_{12} = \frac{1}{2} \left[(E_{12} + K_{122}y + \frac{x}{2} K_{112} + \frac{z}{2} K_{123}) + (E_{21} + K_{211}x + \frac{y}{2} K_{212} + \frac{z}{2} K_{213}) \right] + \frac{1}{2} \left(\frac{\partial \tilde{u}_2}{\partial x} + \frac{\partial \tilde{u}_1}{\partial y} \right) \quad (28)$$

$$\varepsilon_{23} = \frac{1}{2} \left[(E_{23} + K_{233}z + \frac{x}{2} K_{213} + \frac{y}{2} K_{223}) + (E_{32} + K_{322}y + \frac{x}{2} K_{312} + \frac{z}{2} K_{323}) \right] + \frac{1}{2} \left(\frac{\partial \tilde{u}_2}{\partial z} + \frac{\partial \tilde{u}_3}{\partial y} \right)$$

$$\varepsilon_{13} = \frac{1}{2} \left[(E_{13} + K_{133}z + \frac{x}{2} K_{113} + \frac{y}{2} K_{123}) + (E_{31} + K_{311}x + \frac{y}{2} K_{312} + \frac{z}{2} K_{313}) \right] + \frac{1}{2} \left(\frac{\partial \tilde{u}_1}{\partial z} + \frac{\partial \tilde{u}_3}{\partial x} \right)$$

The stationarity condition of the functional on the right-hand side of Eq.(11) delivers as a necessary condition a BVP to be satisfied by the optimal fluctuation associated to the real displacement field (in the absence of body forces). The formulation of the strain gradient BVP for the displacement fluctuation over the UC subjected to an imposed strain and strain gradient kinematic loading writes as follows:

$$\operatorname{div} \left\{ c_{ijkl}(y) : \left(E_{kl} + K_{klm} y_m + \nabla_{y_l} \tilde{u}_k \right) \right\} = 0 \quad (29)$$

This problem has to be solved for the optimal fluctuation associated to the real displacement field. Inserting into Eq. (29) the fluctuating displacement defined in Eq. (7), we get the first and second gradient unit cell BVP's as the stationarity conditions of the previous functional in Eq. (29), successively:

$$\text{BVP1: } -\operatorname{div} \left\{ c_{ijkl}(y) : \left(E_{kl} + \nabla_{y_l} \left(H_{kmn}^E(y) : E_{mn} \right) \right) \right\} = 0 \quad (30)$$

$$BVP2: -\text{div}\left\{c_{ijkl}(y) : \left(K_{klm} y_m + \nabla_{y_l} \left(H_{klmn}^K : K_{lmn}\right)\right)\right\} = 0 \quad (31)$$

Using the expressions in Eq. (28) for the components of the microscopic strain, and after expanding Eq. (29), we get the unit cell BVP for the first and second gradient behaviors as follows:

$$\int_{\Omega} \left[\begin{array}{c} \left(\lambda_i (\varepsilon_{11} + \varepsilon_{22} + \varepsilon_{33}) (\nabla_x V_x + \nabla_y V_y + \nabla_z V_z) + 2\mu_i (\varepsilon_{11} \nabla_x V_x + \varepsilon_{22} \nabla_y V_y + \varepsilon_{33} \nabla_z V_z) \right) \\ + 2\mu_i (\varepsilon_{12} (\nabla_x V_y + \nabla_y V_x) + \varepsilon_{23} (\nabla_y V_z + \nabla_z V_y) + \varepsilon_{13} (\nabla_x V_z + \nabla_z V_x)) \end{array} \right] d\Omega = 0 \quad (32)$$

with V_x , V_y , and V_z therein the test functions. After solving this unit cell problem for the microscopic fluctuation displacement $\tilde{u}_1, \tilde{u}_2, \tilde{u}_3$ with the kinematic loading conditions E, K imposed on the UC, we construct the macroscopic constitutive law and determine the classical and strain gradient elastic moduli. To have the classical behavior of Cauchy we activate only the macroscopic strain field E_{ij} , for the medium of second gradient we activate the strain gradient field K_{ijk} in this problem, where are integrated in the definition of microscopic displacement fields (Eq. 28). The evaluation of the homogenized macroscopic stresses relies on the Hill-Mandel extended macrohomogeneity condition, stating that the volume average of the microscopic internal work within the UC is equal to the macroscopic internal work of the effective strain gradient continuum Eq. (11):

$$W_M(E, K) = \frac{1}{2} E_{ij} : C_{ijkl}^{hom} : E_{kl} + \frac{1}{2} K_{ijk} : A_{ijklmn}^{hom} : K_{lmn} + E_{ij} (B_{ijklm}^{hom} + B_{ijklm}^{hom,T}) : K_{klm} \quad (33)$$

$$\Sigma_{ij} = \langle \sigma_{ij} \rangle = \frac{\partial W_M(E, K)}{\partial E}; \quad S_{ijk} = \langle \sigma_{ij} \otimes y_k \rangle = \frac{\partial W_M(E, K)}{\partial K} \quad (34)$$

The algorithmic implementation of the 3D strain gradient homogenization is provided in Fig. 3 to synthesize the different steps of the numerical implementation of the method.

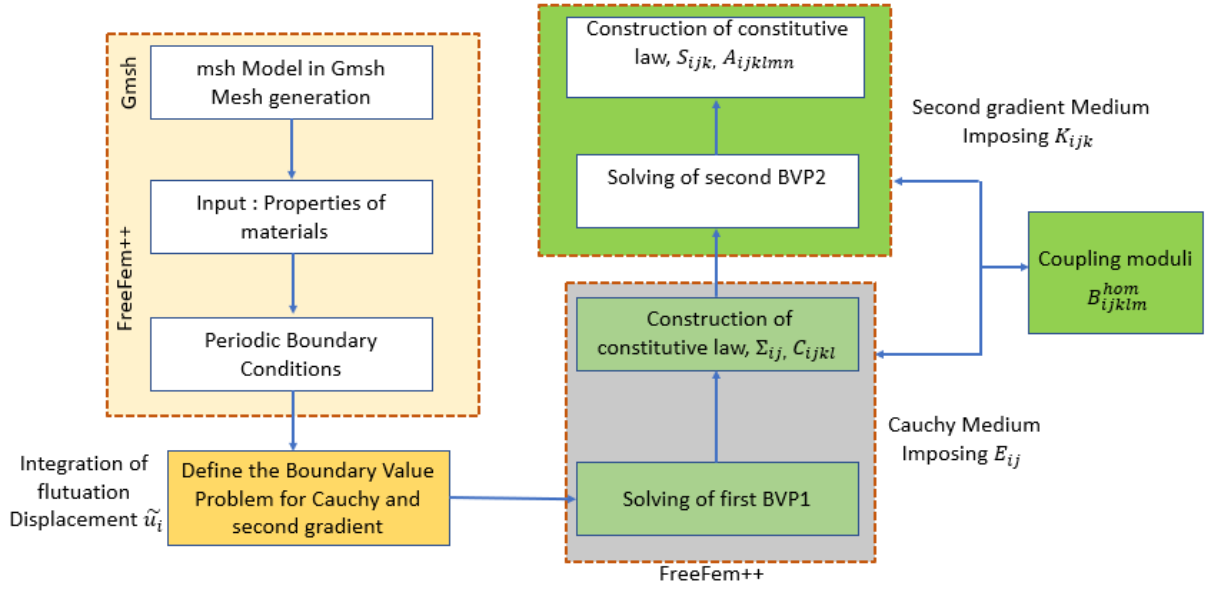


Figure 3: Numerical implementation algorithm.

2.3. Analysis of size effects of the effective Cauchy and second gradient moduli

In order to study possible size effects of the effective higher order elastic moduli in 3D, we set up windows of analysis of different sizes, including increasing repetitions of the UC, from a single UC to four UC's, as shown in Fig. 4. We use the example of composite voided unit cell, the periodicity is applied on the 3 directions x,y and z. A calculation of the effective elastic moduli for Cauchy and second gradient, C_{11}^{hom} and A_{111}^{hom} respectively, has been performed for the composite voided with different sizes of the unit cell.

The second gradient moduli depend on the choice of the unit cell and of the size of the analysis window, the change of the position with respect to the reference of the voids, then of the inclusions in the case of composite materials affects this dependence. Correction terms for the effective strain gradient and coupling moduli are calculated in [21] and more completely with due account of the displacement localization operators in [4], their expression being:

$$\begin{aligned}
 C^{hom*} &= C^{hom} \\
 A^{hom*} &= A^{hom} - C^{hom} \otimes I - H^K \otimes \nabla : H^K \otimes \nabla \\
 B^{hom*} + B^{hom*T} &= -2 C^{hom} \otimes X - 2H^E \otimes \nabla : H^K \otimes \nabla
 \end{aligned} \tag{35}$$

The correction factors have been obtained from the evaluation of the macroscopic energy of a (macro) structure tessellated with unit cells and traduce the need to account for interactions between neighboring unit cells when evaluating the higher gradient moduli.

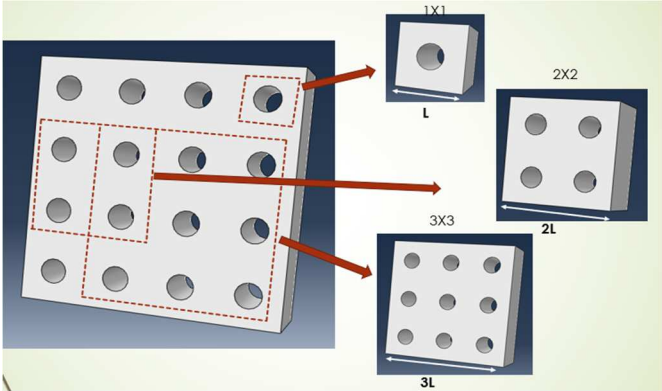


Figure 4 : Size effect of higher gradient moduli within a window of analysis including a single unit cell, 2*2, 3*3 and 4*4 unit cells.

The proposed homogenization method in a 3D context shows a quick convergence of the Cauchy elastic moduli; on the other hand, the strain gradient moduli show a dependency upon the size of the window of analysis, but they converge after a correction factor equal to N^2 is applied, with N the number of repetitions of the UC. The normalized strain gradient moduli $A_{111}^* = A_{111} / N \times N$ show size-independency (fig. 5). The same results have been obtained, but restricted to a 2D context in [4]. The quadratic increase of the strain gradient moduli with the number of unit cells is equivalent to decreasing the unit cell size, considering that the number of unit cells within a macrodomain of fixed area is increased up to the (mathematical) limit of a unit cell of vanishing size. The performed normalization by the factor N^2 is then equivalent to performing the homogenization on a fixed unit cell size so that the absolute unit cell size is absorbed into the normalization process.

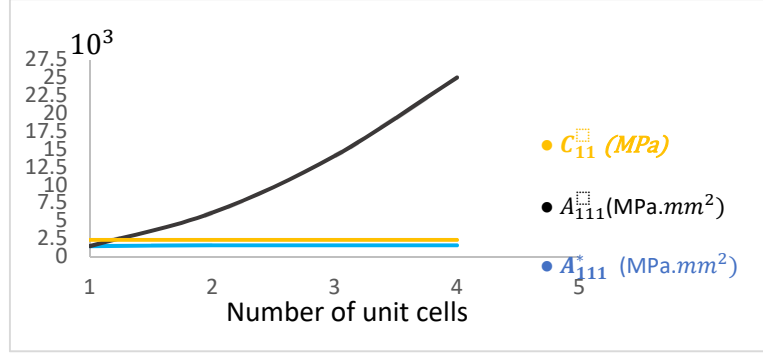


Figure 5 : Second gradient constitutive moduli variation for different UC sizes without correction terms A_{111} and with correction terms A_{111}^* .

2.4. Validation of the effective moduli for composites with a voided unit cell

In order to validate the strain gradient formulation, the response of a heterogeneous microstructure of composites with voids are compared to the response of the strain gradient substitution medium equipped with the effective higher gradient properties computed over its unit cell. We consider an extruded square in-plane domain including a matrix with a void in its center, as pictured in Fig.4(a); the length, width and height parameters of the domain are respectively $L = l = h = 1$ mm and a radius $R = 0.2$ mm is chosen for the void (Fig. 6(a)). The base material is selected to be isotropic with Young modulus and Poisson's ration given successively by $E = 2500$ MPa and $\nu = 0.3$.

A finite element calculation of the mechanical response of the fully resolved microstructured heterogeneous plate shown in Fig. 6(b) is done, with the UC repeated 16 times (16 mm) along the y-direction and 12 times (12 mm) along x-direction. The resulting displacement component u_y is computed with the FE code ABAQUS and is plotted as a function of the material position along the vertical line (from $y = -8$ to $y = 8$ mm in 3D) at the horizontal position $X = 2$ mm to avoid the effects of the domain edges. The same displacement distribution is computed for the homogeneous plate after solving the macroscopic equilibrium to determine the macroscopic displacements U_i of the homogenized plate equipped with the computed effective strain gradient behavior; more precisely, we solve the following equilibrium equation written in weak form with the Freefem++ open source code (the coupling moduli vanish due to the centrosymmetry of the unit cell):

$$\text{div} \Sigma_{ij} - \text{div} S_{ijk} = \text{div} \quad (C_{ijkl}^{hom} : E_{kl}) \quad - \text{div} \quad (A_{ijklmn}^{hom} : K_{lmn}) = 0 \quad (35)$$

The boundary conditions used for both computations (for fully resolved microstructure and the homogeneous plate) with a nil displacement u_x on the vertical edges on the right and on the left edges, and a nil displacement u_y on the lower face of the plate, with a displacement component u_y imposed on the top face $y=L$.

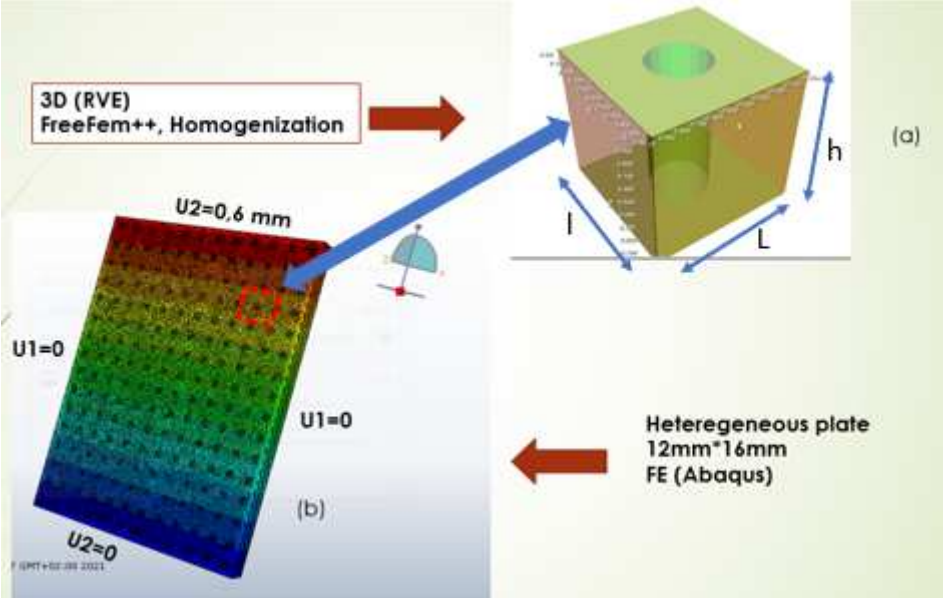


Figure 6: (a) Homogeneous domain and (b) heterogeneous structure including a periodic repetition of the composite UC.

A similar spatial distribution of the displacement is observed for the heterogeneous microstructured domain and the homogeneous domain, calculated from the effective properties of the periodic unit cell, the displacement imposed on the heterogeneous plate on the upper face lies between zero and 0.6 mm.

The microscopic displacement u_y for the heterogeneous domain shows a periodic fluctuation due to the existing voids within the UC, which generates an infinite contrast of microscopic properties. On the other hand, the distribution of the macroscopic displacement within the homogeneous domain is perfectly linear in accordance with the solution of the corresponding linear elasticity BVP, and it increases in the same way as for the heterogeneous plate (Fig. 7).

The present analysis deals with the homogenization towards a Cauchy medium, since uniform boundary conditions are adopted, thus no macroscopic strain gradients are in fact triggered. In subsequent developments, we analyze the response of a pantographic structure for which a macroscopic gradient of the strain is triggered by the application of higher order boundary conditions.

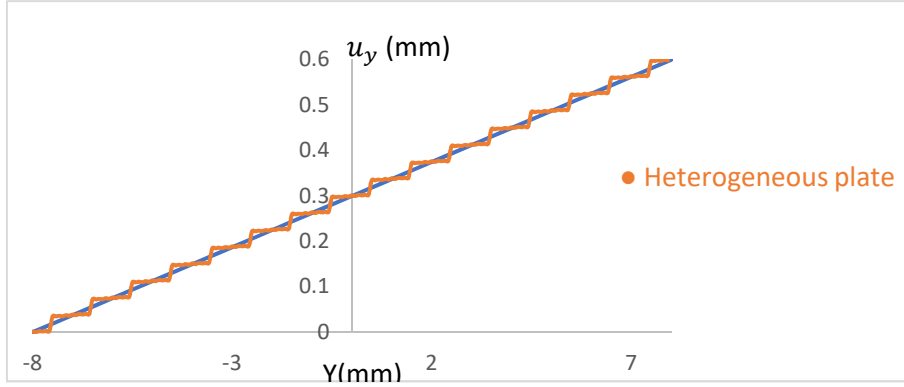


Figure 7: 3D Vertical displacement u_y for the heterogeneous and homogeneous domains along the vertical line y at $x=2\text{mm}$.

In the sequel, the proposed strain gradient homogenization formulation is exemplified by the computation of the effective Cauchy and higher gradient moduli of a selection of 2D and 3D periodic microstructures, addressing especially the issues of size independency, internal lengths computation to quantify the strength of strain gradient effects and activation of strain gradient effects at the macroscale, employing higher order boundary conditions.

3. Strain gradient model of a continuous pantograph

The pantograph is first selected as a structure prone to strong strain gradient effects. A planar pantographic lattice – more details are given in [42,43], [34] is defined as a set of two families of Euler beams, with one family of beams connected by means of an internal pivot to the beams belonging to the other family and intersecting it at a right angle. The pantograph is a well-known typical example of a structure exhibiting no or very little first order elasticity (for inextensible beams), but instead its elastic response appears directly at second order when it is viewed as a continuum (after continualization or homogenization towards an effective continuum has been done), thus it is a second gradient continuum with no Cauchy elasticity. We do here consider instead of the discrete pantograph a continuous version of it, in the form of two orthogonal thick ligaments intersecting at a right angle in the central zone, so that the obtained microstructure has a tetragonal symmetry (Fig. 8). Although the produced microstructure will store deformation energy for Cauchy type elasticity, it is expected to exhibit pronounced strain gradient effects due to the bending of the two intersecting ligaments it is made of.

We start with a 1D analysis of strain gradient effects within a strip including a repetition of the pantograph unit cells to activate macro strain gradients. The dimensions of the unit cell are selected to be $L = l = 10\text{mm}$, thereafter the complete structure made of a repetition of 7 pantograph UC's is characterized by the lengths $L_{1D}=70\text{mm}$, $l_{1D}= 10\text{mm}$, as shown in Fig.8 at UC level and Fig.9 at macrostructural level:

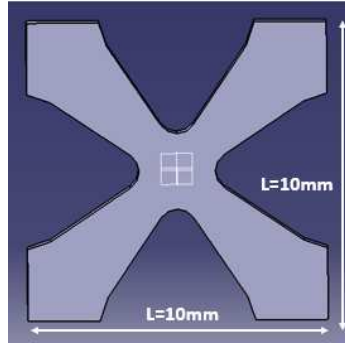


Figure 8: Unit cell of the pantograph.

Boundary conditions in the form of a polynomial and non-homogeneous displacement field are imposed along the x direction on all the faces of the domain of the structure of the pantograph illustrated in Fig. 9. More specifically, we apply the following kinematic higher gradient loading to the unit cell's boundary, $K_{xxx} = \frac{\partial^2 u_x}{\partial x^2} = 1$, in order to trigger uniaxial strain gradient effects along the x-direction. The corresponding displacement boundary conditions imposed over the macrodomain are:

$$u_y = x^2/2; \quad u_y = u_z = 0 \text{ on } \partial\Omega$$

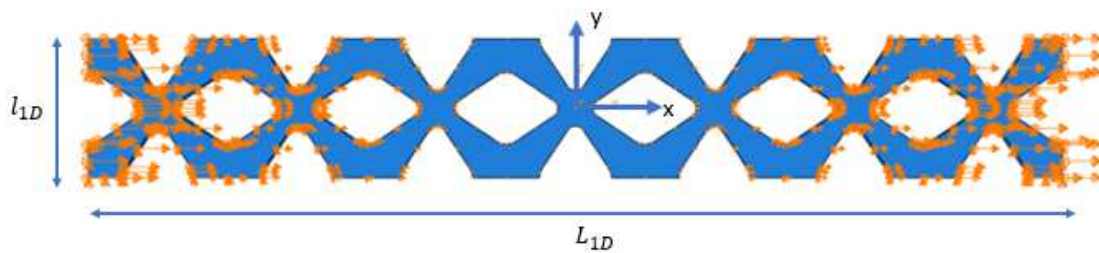


Figure 9: Boundary conditions to trigger strain gradient effects along x direction.

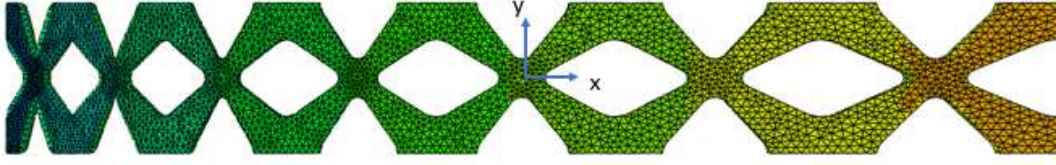


Figure 10: Distribution of strain over the deformed mesh of the pantograph.

The deformed pantograph shape (Fig. 10) underlines the gradient of elongation of the successive UC's from the left edge (fixed along X) to the right edge of the macroscopic sample, with the individual UCs undergoing mostly local bending of their constitutive ligaments. The macroscopic strain reconstructed as the volume average of the microscopic strain shows a quasi-linear variation along the structure, as evidenced in Fig.11 (blue line). The same boundary conditions of second gradient ($u_y = x^2/2$; $u_y = u_z=0$ on $\partial\Omega$) are applied to the homogeneous plate which integrates the homogenized behavior of an elementary pantograph cell, after solving the macroscopic equilibrium (Eq. 35) to determine the macroscopic displacements U_i , thereafter the strain field of the homogenized plate equipped with the computed effective strain gradient behavior. This problem is solved in weak form with Freefem++ open source code.

A similar spatial distribution of the strain component E_{11} along a line crossing the centers of each elementary cell within the heterogeneous plate is obtained as for the homogeneous plate equipped with the effective Cauchy and strain gradient moduli (the macroscopic equilibrium Eq.(35) has been solved), as shown in Fig.11. This confirms the good accuracy of the developed strain gradient model for this pantographic structure.

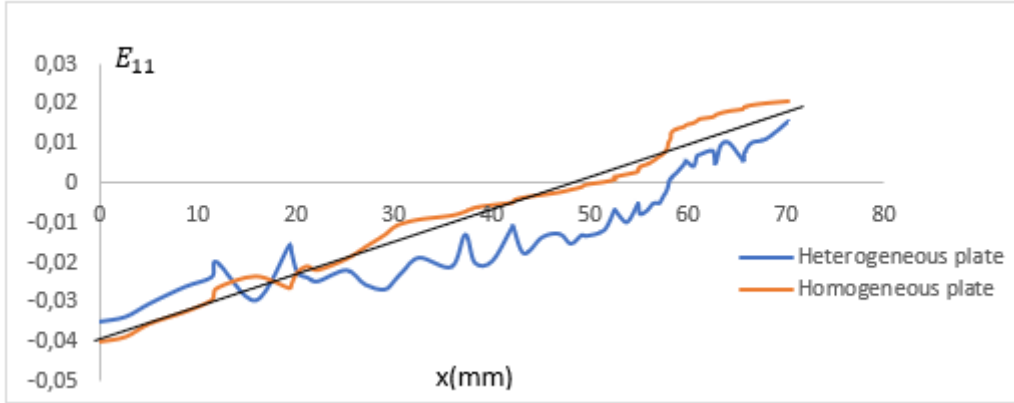


Figure 11: Evolution of the macroscopic deformation in tension along a path line.

The same analysis is next performed for a 2D repetitive pantographic structure shown in Fig.12, repeated 7×7 times in x and y directions in order to perform fully resolved computations of the apparent properties of the pantograph, with the objectives to trigger strain gradient effects.

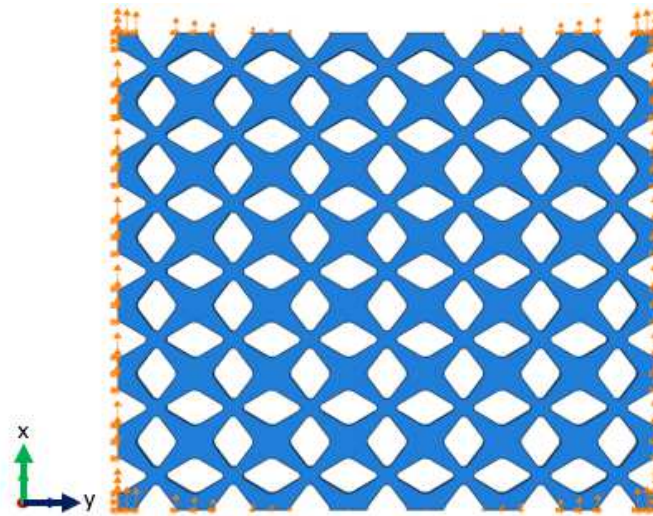


Figure 12: Boundary conditions of second gradient type applied over the pantograph.

The following kinematic higher gradient loading is applied over the unit cell's boundary,

$K_{yyy} = \frac{\partial^2 u_y}{\partial y^2} = 1$ in order to trigger uniaxial strain gradient effects along the y -direction, thus

the corresponding boundary conditions imposed over the macrodomain are:

$$u_y = y^2/2; \quad u_x = u_z = 0 \text{ on } \partial\Omega$$

This kinematic loading reflects the external non-standard external (boundary) forces needed to trigger internal strain gradient effects. It is thus of interest in order to interpret the virtual traction test of the pantograph, recalling the expression of the work of external forces for a strain gradient continuum (obtained by homogenization), including Cauchy tractions, surface double tractions and edge tractions. These last two forces specific to the strain gradient medium enter the expression of the virtual work of external forces equal and opposite to the work of internal forces [8,44] viz the following equality traducing the virtual work principle, with δW_{int} , δW_{ext} the virtual works of internal and external forces successively expressing as:

$$\begin{aligned}
-\delta W_{\text{int}} + \delta W_{\text{ext}} &= 0 \\
\delta W_{\text{int}} &= \int_V (\sigma_{ij} \delta \varepsilon_{ij} + S_{ijk} \delta K_{ijk}) dV \\
\delta W_{\text{ext}} &= \int_S P_k \delta u_k dS + \int_S R_k D \delta u_k dS + \int_C E_k \delta u_k dS
\end{aligned} \tag{36}$$

The quantities P_k, R_k, E_k therein are respectively the surface tractions, the surface double tractions and the edge tractions. The external forces balance the Cauchy stress and hyperstress (the double bracket $\llbracket \cdot \rrbracket$ stands for the jump of the enclosed quantity) as

$$\begin{aligned}
P_k &= n_j (\sigma_{jk} - S_{ijk,i}) - D_j (n_i S_{ijk}) + (D_l n_l) n_j n_i S_{ijk} \\
R_k &= n_i n_j S_{ijk} \\
E_k &= s_m e_{mlj} \llbracket n_l n_j S_{ijk} \rrbracket
\end{aligned} \tag{37}$$

with e_{mlj} the components of the permutation tensor, and s_m the components of the surface vector. The occurrence of these forces involves contributions, which are specific to second gradient continua and it leads to specific features like boundary layers and concentrated forces [34]. The previously applied second order polynomial kinematic loading leads to double reaction forces on the domain edges and corner contributions, corresponding successively to the double force R_k and corner force E_k - here reaction forces due to the imposed displacement -, triggering the deformed shape of the pantograph structure shown in Fig.10. The spatial distribution of the displacement is plotted over the deformed configuration in Fig.13, the shape of which showing a dominant bending deformation of the micro and macrostructures.

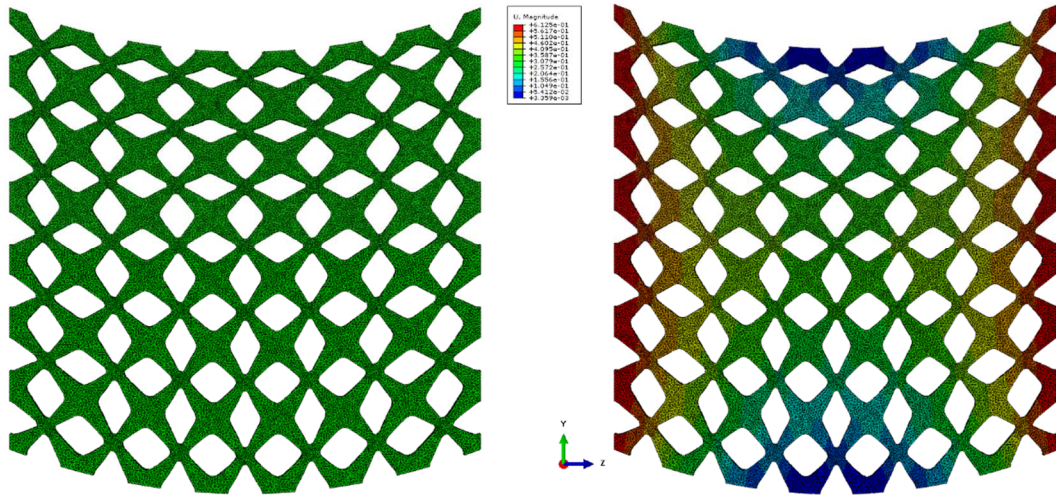


Figure 13: Deformed shape and displacement magnitude of the pantograph structure.

The macroscopic strain component E_{22} is plotted along the path line along the line $x = 3.5$ mm (crossing all elementary cell edges from y_{min} to y_{max}), showing a linear increase along this line (Fig.14), with superimposed significant microscopic fluctuations arising when crossing the successive pantographic UC. A similar behavior is obtained for the uniaxial strain component E_{11} plotted along the same path line in Fig. 15.

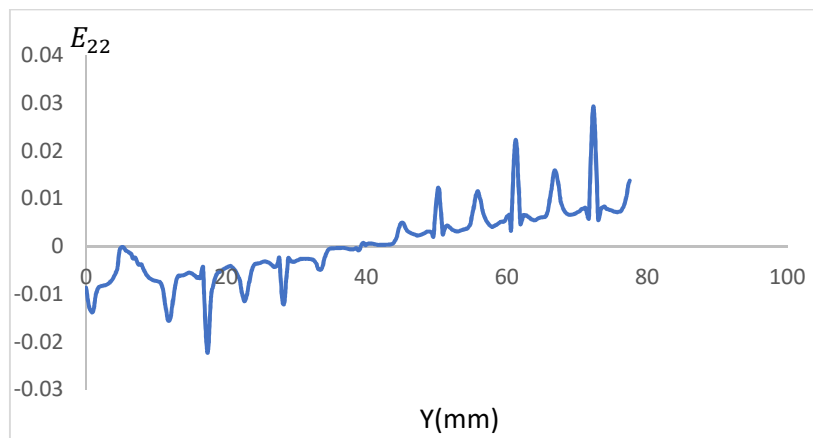


Figure 14: Evolution of the strain component E_{22} along a vertical path line $x=3.5$ mm.

The application of the non-homogeneous boundary conditions results in a linear evolution of the macroscopic strain along the same path line.

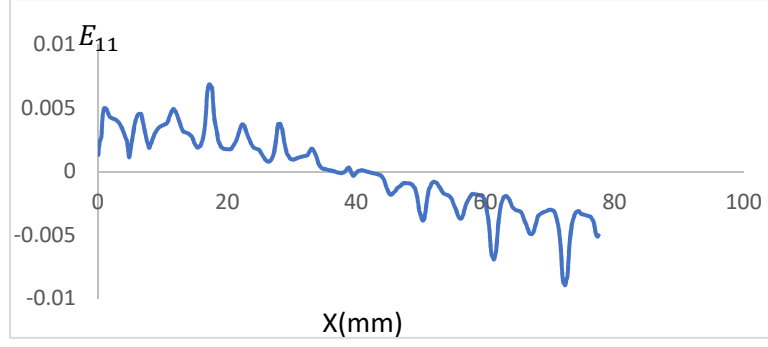


Figure 15: Evolution of the strain component E_{11} along a path line.

We thus have triggered a macroscopic strain gradient within the macrostructure, as it is expected for such a strain gradient effective continuum. Few analyses in the literature show such macroscopic strain gradient effects for composite materials, with the strain gradient contributions arising from the developed internal strain within the repetitive unit cell. This is due to the fact that these macroscopic gradients have to be triggered by suitable higher order boundary conditions as the previous analysis shows; application of classical tractions does not trigger such strain gradient effects. Moreover, in order to complete the argumentation, it is worthwhile mentioning that macroscopic strain gradient are expected to arise as a consequence of the microscopic strain gradients on due account of the classical form of the averaging theorem [45,46]. According to this theorem and for a two-phase material with continuity of displacement and tractions, it holds for any quantity ψ_a

$$\langle \nabla_y \psi_a \rangle_y = \nabla_x \langle \psi_a \rangle_y \quad (38)$$

with $\langle \psi_a \rangle_y$ deserving the name of phase average (the subscripts indicates the scale at which the averaging is done) and defined explicitly as

$$\langle \psi_a \rangle_y = \frac{1}{|Y|} \int_Y \psi_a dV_y \quad (39)$$

We compute the elastic moduli of Cauchy and the gradient of strain for the pantograph unit cell (Fig. 6) for all the deformation modes defined by the strain components E_{ij} and strain gradient components K_{ijk} . We adopt the following microscopic elastic properties of the base material: Young modulus $E=2500\text{MPa}$ and Poisson's ratio $\nu = 0.3$.

Table 1: Calculated equivalent classical moduli C_{ij} for the simulated pantographic structure.

Stiffness component C_{ij} (MPa)	Uniaxial tensile tests			Biaxial tensile tests			Shear tests		
	C_{11}	C_{22}	C_{33}	C_{12}	C_{23}	C_{13}	C_{44}	C_{55}	C_{66}
Pantographic structure	588.4	588.4	1509.9	896	621	621	5.4	151.4	5.4

Table 2: Equivalent second-order stiffness tensor components A for the simulated pantographic structure, Units in N.

A_{111}	A_{222}	A_{333}	A_{122}	A_{133}	A_{211}	A_{233}	A_{311}	A_{322}	A_{112}
11724,36	11724,36	8,56	3788,8	2,48	3788,93	2,488	4040,7	4040,7	13968,9
A_{113}	A_{123}	A_{212}	A_{213}	A_{223}	A_{312}	A_{313}	A_{323}		
13969,1	8086,01	4049,4	4044,04	15547,4	4044,065	4049,596	15548,1		

From the effective Cauchy and second gradient effective moduli, we evaluate the internal lengths in the extension modes in Table 3 to quantify the strength of strain gradient effects at the macroscopic level, basing on Eq. (24) for the definition of internal lengths in strain gradient mechanics.

Table 3: Internal lengths of the pantograph structure.

le_{11} (mm)	le_{22} (mm)
8.7	8.7

We observe that the computed internal lengths are of the same magnitude as the length of the elementary unit cell (here 10mm). These results allow concluding that the pantographic structure shows a very important second gradient effect, in accordance with the literature on the topic.

4. Geometrical and material sensitivity of the second gradient moduli of functionally graded composite structures

In order to study the impact of the geometrical and mechanical microstructural parameters on the effective behavior of 3D composites structures, a macroscopic composite domain including a polymer matrix reinforced by 10 circular inclusions with three different spatial distributions has been designed. The dimensions of the domain are the same for the three selected configurations, namely $L = 3\text{mm}$, $l = 1\text{mm}$ and $h = 1\text{mm}$ (Fig. 16). The first configuration on the left view of Fig.16 has equidistant fibers with the same fiber radius of 0.12 mm ; in the second situation, the distance between fibers is unchanged but the radius of the fibers varies linearly from 0.05mm to 0.18mm . The third configuration exhibits an increasing distance between the fibers at constant radius equal to 0.12mm . Accordingly, the last two configurations are prone to trigger strain gradient effects due to the gradient of morphology of the inherent microstructure. The same number of inclusions inside the matrix is kept for the three cases. The following matrix and fiber properties are adopted: $E_m = 500\text{ MPa}$, $E_f = 2500\text{ MPa}$, with the same Poisson's coefficient for fiber and matrix, $\nu_f = \nu_m = 0.3$. Boundary conditions are applied as in [36] over the macrodomain to determine the equivalent classical and second-order stiffness tensor components (no more periodicity conditions hold).

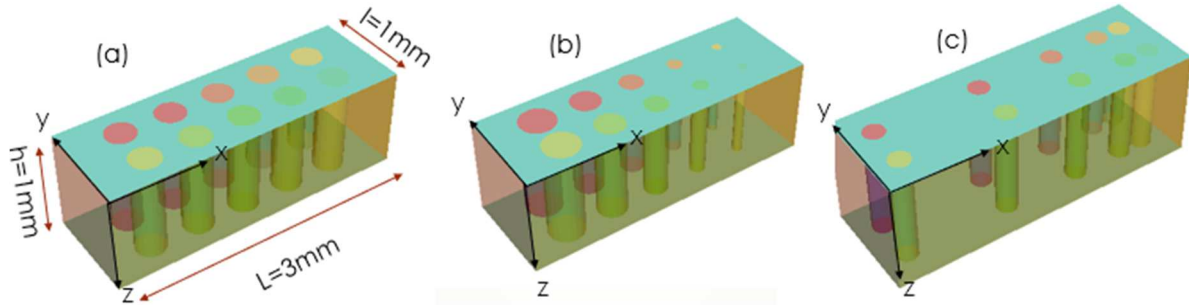


Figure 16: Composite materials with (a) periodic inclusions (b) varying inclusion radius (c) varying of inclusion spacing along x

We observe that configuration (b) has the highest Cauchy effective moduli with the highest volume fraction of the inclusions (Table. 4); on the other hand, configuration (c) with a varying distance between the inclusions shows the highest longitudinal second gradient modulus A_{111} . As expected, the geometric variation (Fig. 16c) along the x-direction generates more pronounced strain gradient effects compared to the situation without geometrical contrast of the microstructure. In the three considered cases, the Cauchy moduli hardly change

(by 3% in relative variation), whereas the geometrical variation of the microstructure within the composite increases second gradient effects as shown by the increasing values of strain gradient moduli and internal length in extension in Table 4. The tensile strain gradient modulus along the x-direction showing geometrical variation show the highest variation (about 5%) as one would expect.

Table 4: Few first and second gradient moduli versus volume fraction of inclusions for the three cases (a), (b) and (c) shown in Fig.16.

	Case (a)	Case (b)	Case (c)
Volume fraction of inclusions V_f	0.15	0.163	0.15
C_{11} (MPa)	1033	1064	1034
C_{12} (MPa)	442.95	456	443
A_{111} (MPa.mm ²)	686	717	827
A_{222} (MPa.mm ²)	71	73	71
A_{333} (MPa.mm ²)	344.5	354.9	344.9
le_{11} (mm)	0.81	0.82	0.89

In the following figures, all strain gradient deformation modes for the different applied kinematic loadings K_{ijk} are shown for the configuration (a) in Figs. 17, 18.

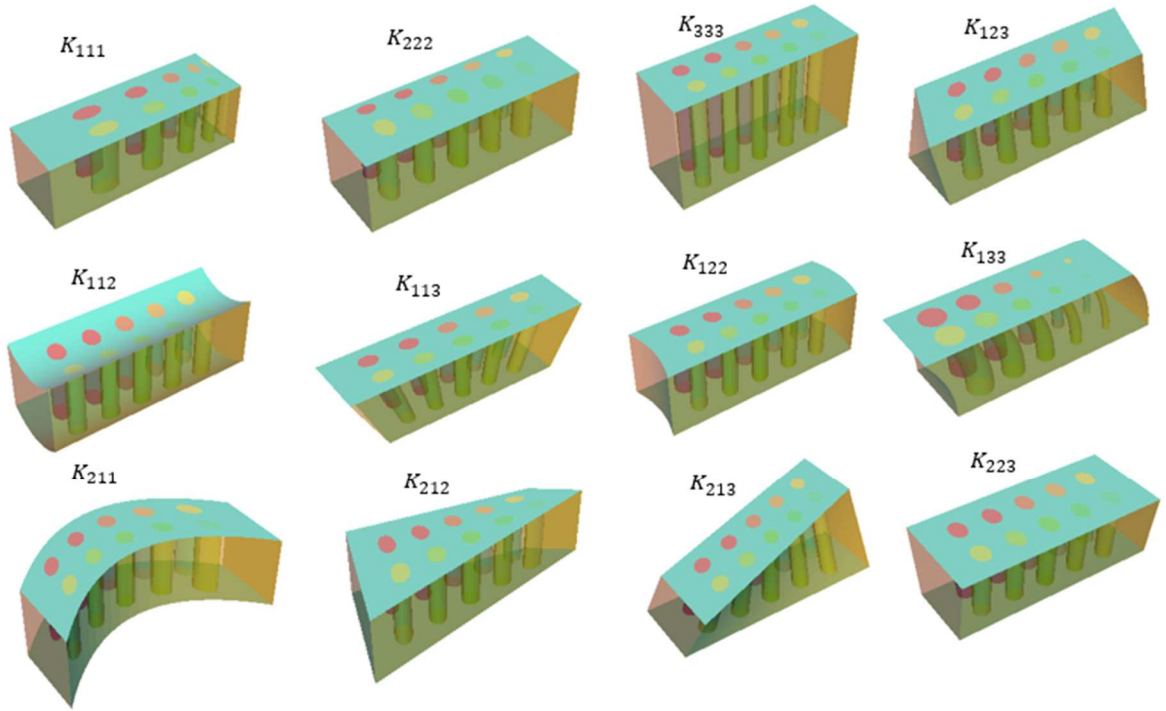


Figure 17: Deformation modes induced by the imposed macroscopic gradient of deformation, part 1.

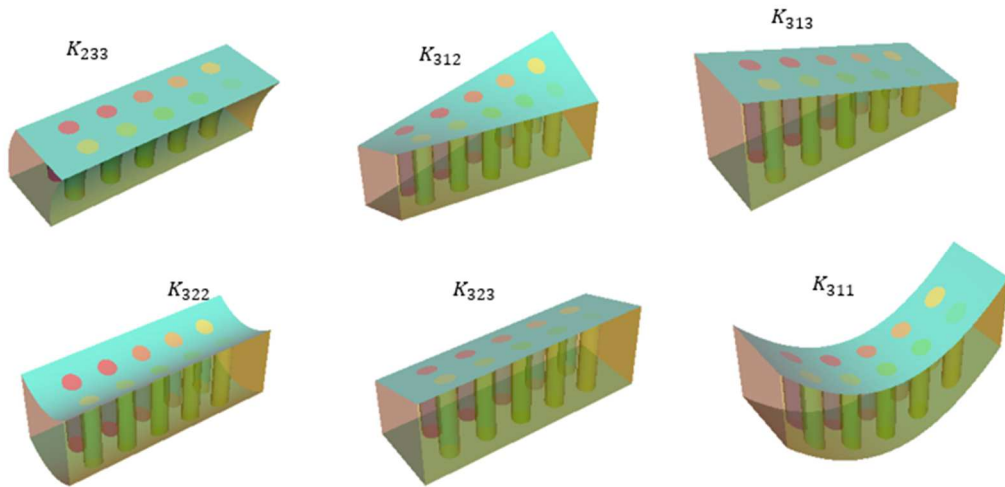


Fig. 18. Deformation modes induced by the imposed macroscopic gradient of deformation, part 2.

In order to quantify the effect of the contrast of the mechanical properties of both constituents on the effective behavior of the studied composite material, a variation of the ratio of the inclusion to matrix Young moduli (E_f/E_m) is considered for the microstructure of case (a) in Fig. 16. The evolution of the effective first and second gradient moduli with

respect to the ratio of moduli is shown in Fig. 19, highlighting an increase of the effective moduli with the stiffness ratio.

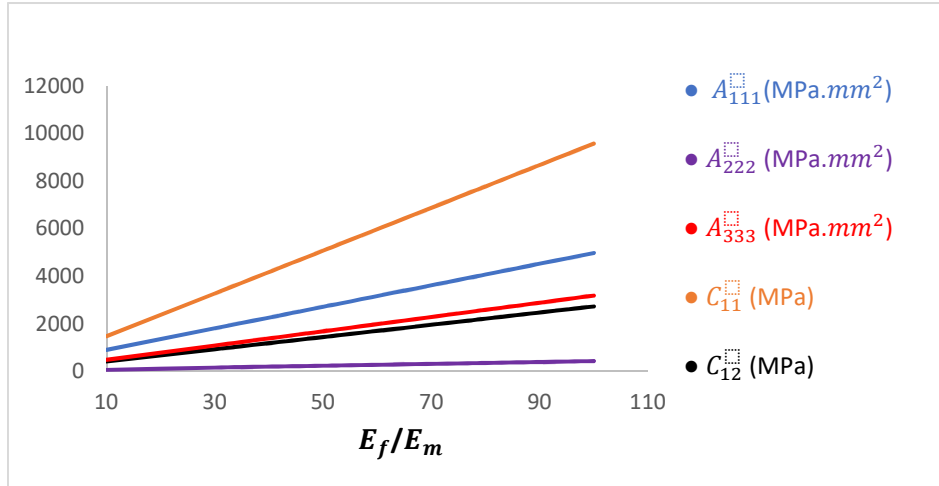


Figure 19: First and second gradient effective moduli in function of the ratio of the inclusion to matrix Young moduli.

The effective moduli A_{111} , A_{222} , A_{333} , A_{113} and C_{11} show a linear increase with the volume fraction of fibers, illustrated in Fig. 20.

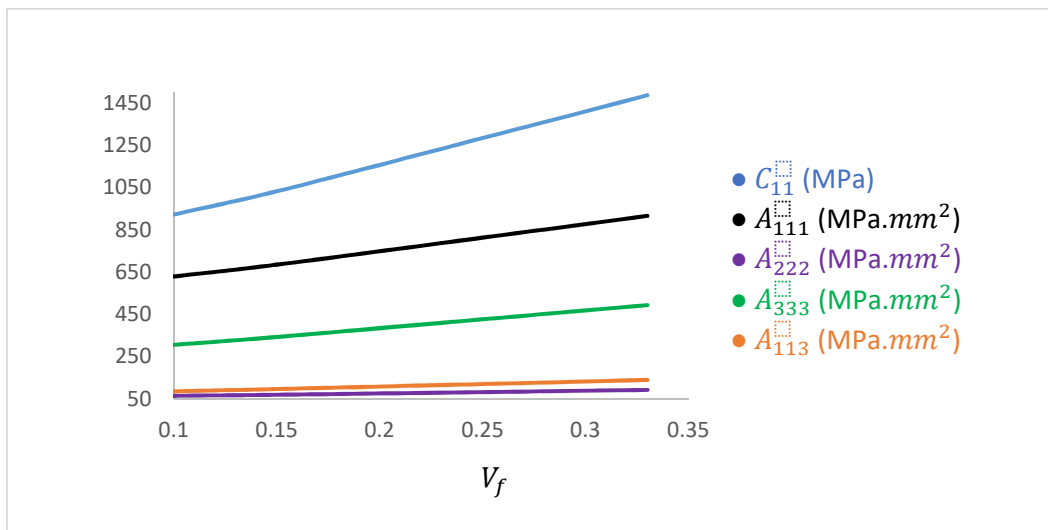


Figure 20: Evolution of first and second gradient moduli with respect to volume fraction of inclusions V_f .

We next analyze the influence of the elasticity ratio of the matrix to the inclusion on the internal length parameters le_{ij} . We use the formulation developed in Section 2 to compute the first and the second gradient constitutive parameters for the composite structure in Fig. 16 case (a), for different elasticity ratio (from 1 to 200) and for a fiber radius $R=0.12$ mm.

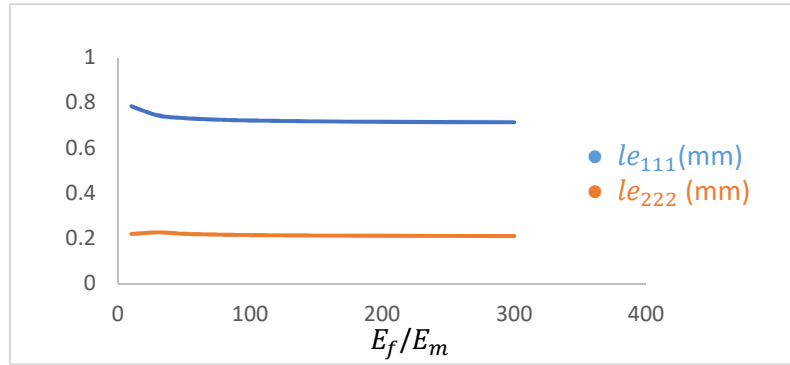


Figure 21 : Variation of internal length parameters le_{ij} as function of the microscopic elasticity ratio E_f/E_m for a fiber radius $R = 0.1\text{mm}$.

We observe that the internal lengths in the two directions x and y , denoted le_{11} and le_{22} show a small variation versus the ratio of microscopic moduli, thereafter a stable value is reached above a ratio of moduli equal to 50. The converged value of the two internal lengths represents 10% and 25 % of the unit cell size.

5. Applications to thin-walled lattice materials

A particularly interesting class of cellular architected materials are the triply periodic minimal surfaces (TPMS) lattice structures. The TPMS architectures allow creating cellular structures having a larger surface area to volume ratio than common strut based cellular structures [47,48]. They have shown attractive multi-functional properties because of its complicated geometries and scale effects [49]. They hold great potential in revolutionizing many engineering applications such as tissue engineering and catalytic substrates. Moreover, the advent of additive manufacturing (AM) has shown to be a viable method for fabricating complicated models such as shell-based TPMS [50] which has accelerated the research on thin-walled TPMS applications. The decrease in surface thickness indicates an increase in porosity, resulting in a biocompatible, biodegradable tissue structure that is both surface and structurally compatible [51]. One of the most common TPMS lattices that are used to build structures with robust mechanical performances is the Gyroid. For example, [52] investigated the energy absorption and failure mechanisms of the Gyroid structure made of Al-Si10-Mg. In addition, [53] has proposed to use Gyroid made of 3D porous graphene to achieve lightweight structural materials with low and density-insensitive thermal properties and superior

mechanical strength. In this section, we aim at evaluating the strain gradient response of the sheet network type Gyroid cellular structure shown in Fig. 22. The generation of such thin-walled lattice is done by applying a constant thickness to an implicit surface. This structure presents strong geometrical variations like curvatures, and is only realizable in 3D space, implying that a 3D strain gradient model is essential. The objective of the subsequent computations is therefore to assess the presence of second gradient effects in this kind of geometries and capture its higher order effects, and subsequently compare the effective first and second order elastic moduli for different unit cell sizes at constant material volume fraction. Herein, the computation methodology is based on the decomposition of the microscopic displacement into a homogeneous and a periodic fluctuation part [4]. This strategy combines a variational formulation and displacement fluctuation that modulates the macroscopic displacement into the calculation of the effective first and second gradient moduli, correcting for the only homogeneous quadratic part of the displacement.

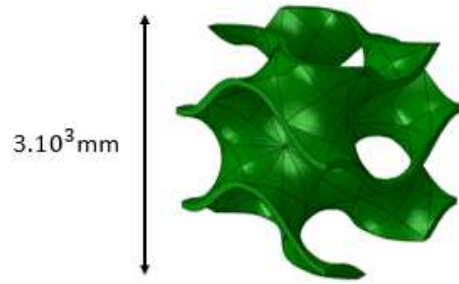


Figure 22 : Unit cell of the Gyroid

We first calculate the effective second gradient moduli for the unit cell of the gyroid (Fig. 22), with the gyroid length, width and height all equal to 3.10^3 mm. The same properties adopted in the previous applications are employed here to be able to compare the internal lengths between the three microstructures, namely Young modulus $E = 2500$ MPa and a Poisson's ratio $\nu = 0.3$. The volume fraction of the gyroid is 0.101, the void volume is $2.42.10^{10} \text{ mm}^3$, thus the volume occupied by the material is $2.73.10^9 \text{ mm}^3$. The computed first and second gradient moduli of the gyroid are given in Tables 5 and 6.

Table 5: Effective Cauchy moduli of the Gyroid

Stiffness coefficients	Uniaxial tensile tests			Biaxial tensile tests			Shear tests		
	C_{11}	C_{22}	C_{33}	C_{12}	C_{23}	C_{13}	C_{44}	C_{55}	C_{66}

$C_{ij}(\text{MPa})$									
Gyroid	7489.02	7489.02	7489.02	3209.58	3209.58	3209.58	2139.72	2139.72	2139.72

Table 6: Effective second gradient moduli of the gyroid, Units in N.

A_{111}	A_{222}	A_{333}	A_{122}	A_{133}	A_{211}	A_{233}	A_{311}	A_{322}
$2.24 \cdot 10^{10}$	$2.24 \cdot 10^{10}$	$9.77 \cdot 10^9$	$6.4 \cdot 10^9$	$2.79 \cdot 10^9$	$6.4 \cdot 10^9$	$1.39 \cdot 10^9$	$6.4 \cdot 10^9$	$6.4 \cdot 10^9$
A_{112}	A_{113}	A_{123}	A_{212}	A_{213}	A_{223}	A_{312}	A_{313}	A_{323}
$1.12 \cdot 10^{10}$	$4.88 \cdot 10^9$	$1.39 \cdot 10^9$	$3.2 \cdot 10^9$	$1.39 \cdot 10^9$	$4.88 \cdot 10^9$	$3.2 \cdot 10^9$	$1.39 \cdot 10^9$	$1.39 \cdot 10^9$

In order to quantify strain gradient effects for the gyroid, its internal lengths are evaluated in Table 7.

Table 7: Internal lengths of the gyroid with normalized values

Internal lengths (mm)	le_{11}	le_{22}	le_{33}
Gyroid UC	2053.82	2007.79	1736

The internal lengths represent 68% of the gyroid unit cell length (indicated in Fig. 22), thereby showing that the gyroid shows important strain gradient effects, due essentially to the bending deformation modes of its cell walls.

The effective moduli of gyroids having different sizes (number of repetitions of the UC) are computed in order to test the convergence of the moduli versus the model size (three repetitions of which are shown in Fig. 23).

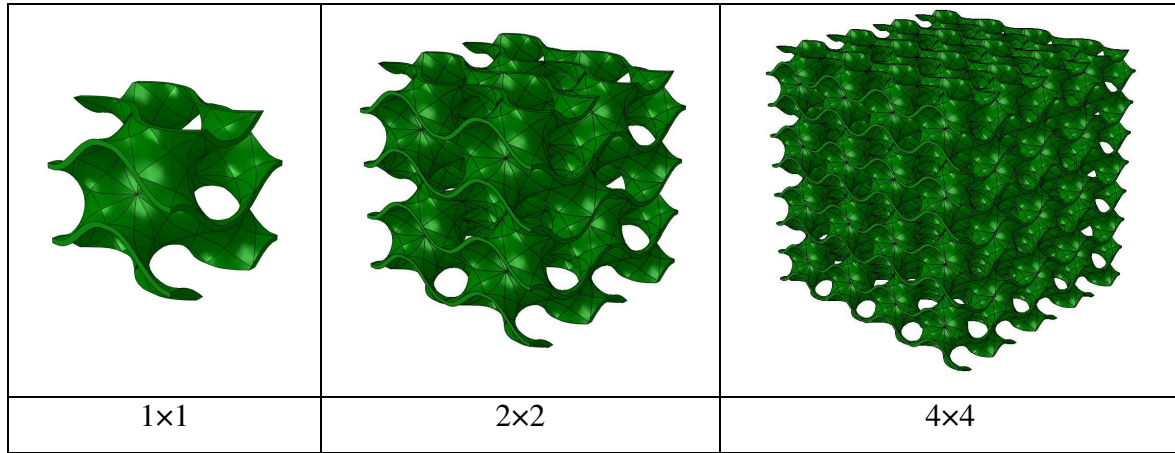


Figure 23: Gyroid window of analysis of different sizes.

Table 8: Volume fraction and porosity for different numbers of unit cell

	V_m ($10^9 mm^3$)	Porosity ($10^9 mm^3$)	A_{111} (MPa. mm^2)	A_{222}	A_{333}
N=1	2.73	24.27	$2.24 \cdot 10^{10}$	$2.24 \cdot 10^{10}$	$9.77 \cdot 10^9$
N=2	21.19	194.87	$2.27 \cdot 10^{10}$	$2.27 \cdot 10^{10}$	$9.8 \cdot 10^9$
N=4	126.9	1728.5	$2.28 \cdot 10^{10}$	$2.28 \cdot 10^{10}$	$9.81 \cdot 10^9$

We observe that the strain gradient moduli remain stable when increasing the size of the UC, with a very small variation, so no size effect is observed. Some modes of deformation associated to second gradient moduli for the gyroid are shown in Fig.24 for a three unit's repetition of the UC for the purpose of the visualization of the deformed shape, considering that the gyroid is a very porous structure.

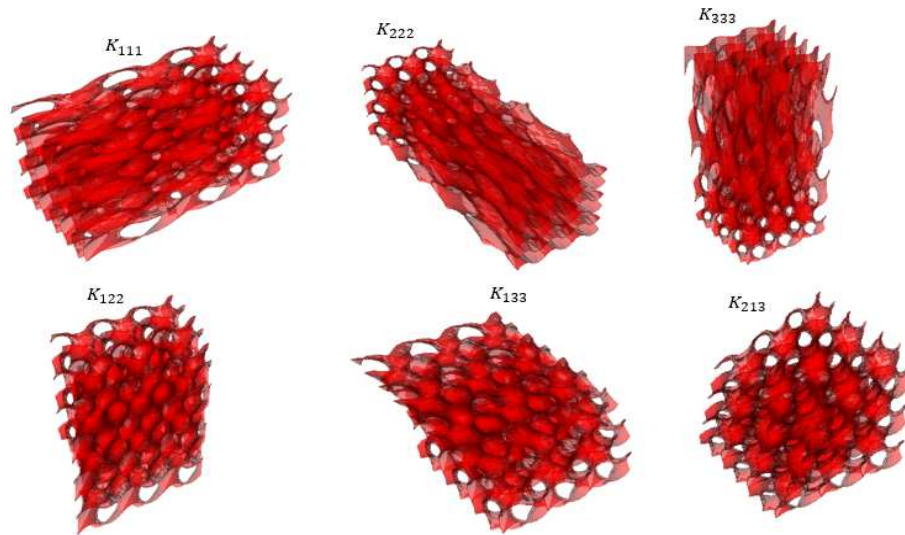


Figure 24: Microscopic deformation modes induced by the imposed gradient of deformation of the gyroid with a repetition of $N=3$ unit cells.

To summarize the results obtained for the three considered microstructures, namely the pantograph, fiber reinforced composites and the gyroid, the normalized internal length (by the length of the elementary cell) are shown in Fig. 25.

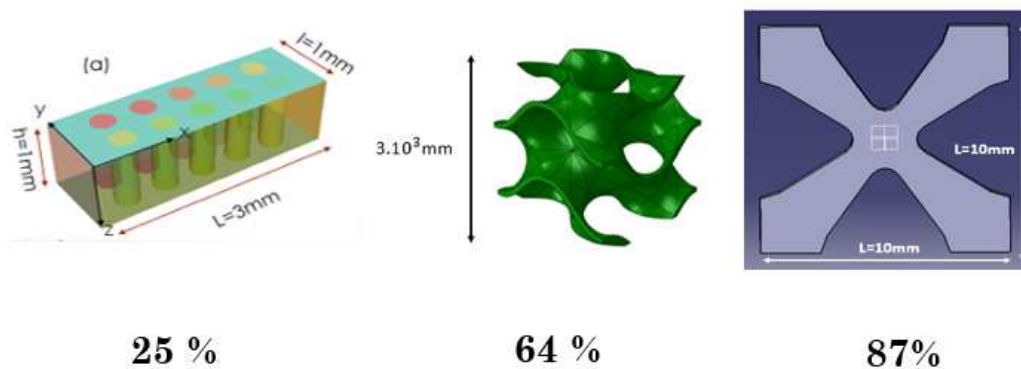


Figure 25: Percentage of internal length in relation to the length of the elementary cell for the three studied microstructures.

Based on this measure, the pantograph and the gyroid are prone to large strain gradient effects (their internal length being close to the unit cell size), whereas inclusion based composites show a comparatively lesser second gradient effect since their internal length only represents 25% of the unit cell length.

6. Conclusion

This paper proposes a strain gradient homogenization method for heterogeneous materials in a 3D context for microstructures that cannot be projected in 2D, of which there very few in the literature. The developed 3D higher strain gradient formulation proves necessary for microstructures that have a true 3D geometry such that the spatial distribution of constituents influences the macroscopic behavior in all three directions.

The formulated homogenization method remedies two important limitations of the existing works of the literature devoted to higher order homogenization of heterogeneous materials: the lack of convergence of the strain gradient moduli with the UC size and the persistence of higher order properties in conditions of perfect scale separation [54-57], [17], [36], [38]. Previous authors employ kinematic quadratic boundary conditions for the microscopic displacement imposed over the UC to capture the higher order moduli, but they do not incorporate the fluctuating part of the displacement that corrects for the difference between the postulated homogeneous strain gradient continuum and the heterogeneous microstructure. Therefore, the computed strain gradient moduli do show a pronounced size-dependency and even sometimes do not converge to stable values when increasing the number of repetitions of the unit cell. Our formulation is based on a variational principle and the microscopic displacement accounts for both the homogeneous polynomial contribution incorporating the macroscopic kinematic variables and a fluctuating term solving two sequential unit cells boundary value problems. The developed strain gradient method shows an independency of the effective moduli to the unit cell size and absolute dimension when normalizing the strain gradient effective moduli by the square of the number of unit cells and accounting for correction terms reflecting interactions between neighboring unit cells.

The performed analyses have shown that the internal length parameters are strongly dependent on the geometrical microstructure properties, the fraction of inclusion, whereas the elasticity ratio between the matrix and the inclusion has a lesser impact on the internal lengths, which are converging for high contrast of elastic moduli. For small volume fractions of reinforcement and mechanical contrast, the classical first gradient formulation is sufficient to describe the composite macroscopic behavior.

In terms of perspectives, the proposed homogenization method can potentially handle a wide diversity of regular 2D and 3D composites and architected materials for which strain gradient models can be identified in future developments.

Data availability

The raw and processed data required to reproduce these findings are available in the successive Tables and figures of the present paper.

References

- [1] Mindlin RD, Eshel NN. On first strain-gradient theories in linear elasticity. *Int J Solids Struct*, 1968 4(1) 109-124.
- [2] C. W. Lim, G. Zhang, J. N. Reddy. A higher-order nonlocal elasticity and strain gradient theory and its applications in wave propagation, *J. Mech. Phys. Solids*, 2015, 78, 298-313.
- [3] Ayad M, Karathanasopoulos N, Ganghoffer JF, Lakiss H. Higher-gradient and micro-inertia contributions on the mechanical response of composite beam structures. *International Journal of Engineering Science*, Volume 154, September 2020, 103318.
- [4] Ganghoffer JF, Reda H. A variational approach of homogenization of heterogeneous materials towards second gradient continua, *J Mechanics of Materials*. Volume 158, July 2021, 103743.
- [5] Cosserat E, Cosserat F. *Théorie des corps déformables*. Herman et Fils, Paris. 1909.
- [6] Eringen AC, Suhubi ES. Nonlinear theory of simple micro-elastic solids—I. *International Journal of Engineering Science*, 1964, 2 (2) 189–203, 389-40.
- [7] R. D. Mindlin, *Micro-structure in linear elasticity*, *Archive for Rational Mechanics and Analysis*, 1964.
- [8] Germain P. The method of virtual power in continuum mechanics. Part 2 : Microstructure. *SIAM J. Appl. Math.*, 1973. 25(3) 556–575, 1973. <https://doi.org/10.1137/0125053>.
- [9] R. Larsson, S. Diebels A second-order homogenization procedure for multi-scale analysis based on micropolar kinematics. *Int. J. Numer. Meth. Engng* 2007; 69:2485–2512.
- [10] Auffray, N., Bouchet, R., Brechet, Y., (2010). Strain gradient elastic homogenization of bidimensional cellular media. *Int. J. Solids Struct*. 47 (13), 1698–1710.
- [11] Berkache K, Deogekar S, Goda I, Picu C. Ganghoffer, JF. Construction of second gradient continuum models for random fibrous networks and analysis of size effects. *Compos. Struct*. 2017, 181, 347–357.
- [12] H. Yang, B. E. Abali, D. Timofeev, W. H. Müller. Determination of metamaterial parameters by means of a homogenization approach based on asymptotic analysis. *Continuum Mech. Thermodyn.* (2020) 32:1251–1270
- [13] dell’Isola, F., Placidi, L.: Variational principles are a powerful tool also for formulating field theories. In: *Variational models and methods in solid and fluid mechanics*, pp. 1–15. Springer, Berlin (2011)

- [14] Tekoğlu, C., Onck, P.R.: Size effects in two-dimensional Voronoi foams: a comparison between generalized continua and discrete models. *J. Mech. Phys. Solids* 56(12), 3541–3564 (2008)
- [15] dell’Isola, F., Giorgio, I., Pawlikowski, M., Rizzi, N.: Large deformations of planar extensible beams and pantographic lattices: heuristic homogenization, experimental and numerical examples of equilibrium. *Proc. R. Soc. A: Math. Phys. Eng. Sci.* 472(2185), 20150, 790 (2016)
- [16] Giorgio, I., Rizzi, N., Turco, E.: Continuum modelling of pantographic sheets for out-of-plane bifurcation and vibration analysis. *Proc. R. Soc. A: Math. Phys. Eng. Sci.* 473(2207), 20170, 636 (2017)
- [17] Kouznetsova, V., Geers, M.G., Brekelmans, W.M.: Multi-scale constitutive modelling of heterogeneous materials with a gradient-enhanced computational homogenization scheme. *Int. J. Numer. Methods Eng.* 54(8), 1235–1260 (2002)
- [18] Tran, T.H., Monchiet, V., Bonnet, G.: A micromechanics-based approach for the derivation of constitutive elastic coefficients of strain-gradient media. *Int. J. Solids Struct.* 49(5), 783–792 (2012)
- [19] Rosi, G., Placidi, L., Auffray, N.: On the validity range of strain-gradient elasticity: a mixed static-dynamic identification procedure. *Eur. J. Mech.-A/Solids* 69, 179–191 (2018)
- [20] Franciosi, P., El Omri, A.: Effective properties of fiber and platelet systems and related phase arrangements in n-phase heterogeneous media. *Mech. Res. Commun.* 38(1), 38–44 (2011)
- [21] Li, J.: A micromechanics-based strain gradient damage model for fracture prediction of brittle materials—Part I: homogenization methodology and constitutive relations. *Int. J. Solids Struct.* 48(24), 3336–3345 (2011).
- [22] Scerrato, D., Giorgio, I., Rizzi, N.L.: Three-dimensional instabilities of pantographic sheets with parabolic lattices: numerical investigations. *Z. Angew. Math. Phys.* 67(3), 53 (2016).
- [23] Nejadi Sadeghi, N., De Angelo, M., Drobnicki, R., Lekszycki, T., dell’Isola, F., Misra, A.: Parametric experimentation on pantographic unit cells reveals local extremum configuration. *Exp. Mech.* 59(6), 927–939 (2019).
- [24] Placidi, L., Barchiesi, E., Turco, E., Rizzi, N.L.: A review on 2D models for the description of pantographic fabrics. *Z. Angew. Math. Phys.* 67(5), 121 (2016).
- [25] Turco, E., Golaszewski, M., Giorgio, I., D’Annibale, F.: Pantographic lattices with non-orthogonal fibres: experiments and their numerical simulations. *Compos. Part B: Eng.* 118, 1–14 (2017).
- [26] Hill R. Generalized constitutive relations for incremental deformation of metal crystals by multislip. *J. Mech. Phys. Solids*, 1966, 14, 95–102.
- [27] Mandel, J., 1966. Contribution théorique à l’étude de l’écrouissage et des lois de l’écoulement plastique. In: *Applied Mechanics*. Springer Berlin Heidelberg, Berlin,

Heidelberg, pp. 502–509. https://doi.org/10.1007/978-3-662-29364-5_67.

[28] Ben-Amoz M. A dynamic theory for composite materials. *Z. Angew. Math. Phys.* 1976, 27 (1), 83–99.

[29] Forest S, Sab K. Cosserat overall modelling of heterogeneous materials. *Mech. Res. Commun.* 1998, 25(4), 449–454.

[30] Forest, S., 1998. Mechanics of generalized continua: construction by homogenization. *J. Phys. IV* 39–48.

[31] Forest S, Pradel F, Sab K. Asymptotic analysis of heterogeneous Cosserat media. *Int. J. Solids Struct.* 2001, 38 (26-27), 4585–4608.

[32] Trinh DK, Janicke R, Auffray N, Diebels S, Forest S. Evaluation of generalized continuum substitution models for heterogeneous materials, *International Journal for Multiscale Computational Engineering*, 2012. 10 (6), 527-549.

[33] Tran TH, Monchiet V, Bonnet G. A micromechanics-based approach for the derivation of constitutive elastic coefficients of strain-gradient media. *Int. J. Solids Struct.* 2012, 49, 783–792.

[34] Rahali Y, Giorgio I, Ganghoffer JF, dell’Isola F. Homogenization à la Piola produces second gradient continuum models for linear pantographic lattices. *Int. J. Eng. Sci.* 2015, 97, 148–172.

[35] Bacigalupo A, Gambarotta L, 2010. Second-order computational homogenization of heterogeneous materials with periodic microstructure. *Journal of Applied Mathematics and Mechanics.* 10 – 11, 796 – 811.

[36] Goda, I., Ganghoffer, J.-F., (2016). Construction of first and second order grade anisotropic continuum media for 3D porous and textile composite structures. *Compos. Struct.* 141, 292–327. <https://doi.org/10.1016/j.compstruct.2016.01.061>.

[37] Bacigalupo A, Gambarotta L. Homogenization of periodic hexa-and tetrachiral cellular solids. *Compos. Struct.* 2014, 116, 461–476.

[38] Berkache, K., Deogekar, S., Goda, I., Picu, R., Ganghoffer, J.-F., (2017). Construction of second gradient continuum models for random fibrous networks and analysis of size effects. *Compos. Struct.* 181, 347–357. <https://doi.org/10.1016/j.compstruct.2017.08.078>.

[39] Bensoussan A, Lions JL, Papanicolaou G. *Asymptotic Analysis of Periodic Structures.* North-Holland, Amsterdam. 1978.

[40] Sanchez-Palencia E. *Non-Homogeneous Media and Vibration Theory*, Springer, Berlin. 1980.

[41] Kröner E. Elasticity theory of materials with long range cohesive forces *International Journal of Solids and Structures*, 1968, 3(5), 731-742.

[42] Madeo A, Della Corte A, Greco L, Neff P. Wave propagation in pantographic 2D lattices with internal discontinuities. *Proceedings of the Estonian Academy of Sciences*, 2015, 64(3S), 325–330.

- [43] F. dell'Isola, U. Andreaus, L. Placidi, At the origins and in the vanguard of peridynamics, non-local and higher gradient continuum mechanics. An underestimated and still topical contribution of Gabrio Piola, 2015b, pp. 885–886.
- [44] Papanicolopoulos SA, Zervos A. Continua with microstructure: Part II: second-gradient theory, *J European Journal of Environmental and Civil Engineering*, 2010. Issue number 1-10, 1031-1050.
- [45] Howes FA, Whitaker S. The spatial averaging theorem revisited. *Chemical Engineering Science* 1985, 40, Issue 8, 1387-1392.
- [46] Wood, B.D., 2013. Technical Note: Revisiting the Geometric Theorems for Volume Averaging.
- [47] D.-J. Yoo. Advanced porous scaffold design using multi-void triply periodic minimal surface models with high surface area to volume ratios, *Int. J. Precis. Eng. Manuf.*, 15 (2014), pp. 1657-1666.
- [48] D.W. Abueidda, R.K. Abu Al-Rub, A.S. Dalaq, D.-W. Lee, K.A. Khan, I.M. Jasiuk. Effective conductivities and elastic moduli of novel foams with triply periodic minimal surfaces. *Mech. Mater.*, 95 (2016), pp. 102-115
- [49] Al-Ketan O., Abu Al-Rub R.K. Multifunctional Mechanical Metamaterials Based on Triply Periodic Minimal Surface Lattices. *Adv. Eng. Mater.* 2019; 21:1900524. doi: 10.1002/adem.201900524.
- [50] Jafari D., Wits W.W. The utilization of selective laser melting technology on heat transfer devices for thermal energy conversion applications: A review. *Renew. Sustain. Energy Rev.* 2018; 91:420–442.
- [51] S. Qu, J. Ding, and X. Song. Achieving Triply Periodic Minimal Surface Thin-Walled Structures by Micro Laser Powder Bed Fusion Process. *Micromachines (Basel)*. 2021 Jun; 12(6): 705.
- [52] I. Maskery, N.T. Aboulkhair, A.O. Aremu, C.J. Tuck, I.A. Ashcroft. Compressive failure modes and energy absorption in additively manufactured double gyroid lattices. *Addit. Manuf.*, 16 (2017), pp. 24-29.
- [53] G.S. Jung, J. Yeo, Z. Tian, Z. Qin, M.J. Buehler. Unusually low and density-insensitive thermal conductivity of three-dimensional gyroid graphene. *Nanoscale*, 9 (2017), pp. 13477-13484.
- [54] Huet, C., 1990. Application of variational concepts to size effects in elastic heterogeneous bodies. *J. Mech. Phys. Solid.* 38 (6), 813–841.
- [55] Kanit, T., Forest, S., Galliet, I., Mounoury, V., Jeulin, D., 2003. Determination of the size of the representative volume element for random composites: statistical and numerical approach. *Int. J. Solid Struct.* 40 (13–14), 3647–3679.
- [56] Forest, S., Trinh, D., 2011. Generalized continua and non-homogeneous boundary conditions in homogenisation methods. *ZAMM-J. Appl. Math. Mech.* 91 (2), 90–109.

[57] Geers, M., Kouznetsova, V., Brekelmans, W., 2001. Gradient-enhanced computational homogenization for the micro-macro scale transition. *J. Phys. IV* 11 (PR5), r5–145.